AD 748993

NRL Report 7434

Behavior of α-β Tracker for Maneuvering Targets Under Noise, False Target, and Fade Conditions

BEN H. CANTRELL

Radar Analysis Staff
Radar Division

August 17, 1972

DDC
RECEIVED
SEP 28 1972
B

NATIONAL TECHNICAL
INFORMATION SERVICE

NAVAL RESEARCH LABORATORY
Washington, D.C.

Approved for public release, distribution unlimited.

Security Classification

DOCUMENT CONTROL DATA - R & D

Security classification of title, body of abstract and indexing annotation must be entered when the overall report is classified

1 ORIGINATING ACTIVITY (Corporate author) Naval Research Laboratory Washington, D.C. 20390	2a. REPORT SECURITY CLASSIFICATION Unclassified 2b GROUP

3 REPORT TITLE

Behavior of α-β Tracker for Manuevering Targets under Noise, False Target, and Fade Conditions

4 DESCRIPTIVE NOTES (Type of report and inclusive dates)
An interim report on a continuing problem.

5 AUTHOR(S) (First name, middle initial, last name)

Ben H. Cantrell

6 REPORT DATE	7a TOTAL NO OF PAGES	7b NO OF REFS
August 17, 1972	52	7

8a CONTRACT OR GRANT NO NRL Prob. R02-54 b PROJECT NO RF 05-151-403-4010	9a. ORIGINATOR'S REPORT NUMBER(S) NRL Report 7434
	9b. OTHER REPORT NO(S) (Any other numbers that may be assigned this report)

10 DISTRIBUTION STATEMENT

Approved for public release; distribution unlimited.

11 SUPPLEMENTARY NOTES	12 SPONSORING MILITARY ACTIVITY Department of the Navy (Office of Naval Research) Arlington, Virginia 22217

13 ABSTRACT

The behavior of the α-β tracker or filter which is found in track-while-scan radars was investigated under various situations. First the target's motion was translated into signals which excite the filter. It was found that these signals could be characterized in terms of target performance capabilities such as velocity, acceleration, and structural loading. Neglecting false alarms and fades, the probability of breaking track was found to depend on the scan time, the measurement noise, the target trajectory, and the parameters α and β. The tracking errors could be categorized into variances and mean errors which were investigated more fully. Using a postulated strategy, the effects of false alarms and fades were found on the variances and mean errors.

1 A

DD FORM 1 NOV 65 1473 (PAGE 1)

S/N 0101-807-6801

Security Classification

Security Classification

14 KEY WORDS	LINK A		LINK B		LINK C	
	ROLE	WT	ROLE	WT	ROLE	WT
α-β tracker						
Track-while-scan radar						
Search radar						

DD FORM 1 NOV 65 1473 (BACK)
(PAGE 2)

Security Classification

CONTENTS

ABSTRACT

The behavior of the α-β tracker or filter which is found in track-while-scan radars was investigated under various situations. First the target's motion was translated into signals which excite the filter. It was found that these signals could be characterized in terms of target performance capabilities such as velocity, acceleration, and structural loading. Neglecting false alarms and fades, the probability of breaking track was found to depend on the scan time, the measurement noise, the target trajectory, and the parameters α and β. The tracking errors could be categorized into variances and mean errors which were investigated more fully. Using a postulated strategy, the effects of false alarms and fades were found on the variances and mean errors.

AUTHORIZATION

NRL Problem R02-54
Project RF 05-151-403-4010

Manuscript submitted April 24, 1972.

BEHAVIOR OF α-β TRACKER FOR MANEUVERING TARGETS UNDER NOISE, FALSE TARGET, AND FADE CONDITIONS

1.0 INTRODUCTION

The subjects of automatic detection and tracking have received a considerable amount of attention in the last several years. For instance, the NTDS, MTDS, and SPS-33 systems are operational, and the Gilfillan Company and Applied Physics Laboratory (APL) systems have been proposed for the SPS-48. These systems have varying degrees of automation, and with the exception of NTDS, have the capability of automatic detection and tracking of targets. The NTDS system, while having tracking equations and correlation regions, depends on a manual updating of tracks.

A system which performs automatic tracking (not detection) is presently being investigated. The automatic tracking system (ATS) operates as follows. Tracks are initiated either by an operator or possibly automatically if clutter is not present. After initialization, an α-β tracker makes smoothed estimates of a target's position and velocity and uses these estimates to predict the target position at the next update time. A correlation region is centered at the predicted position and an automatic detection is made in the correlation region. The advantage of this system (in comparison to other systems) is that there is a high a priori probability of the target being in the small correlation region, and consequently, a much higher false-alarm rate than usual is tolerable. In other words, this procedure avoids system saturation due to the large number of false alarms which would be inherent in a totally automatic detection system. It is believed that a system of this type will be able to track targets through some degree of clutter.

The purpose of this report is to investigate the performance of the α-β tracker when targets are maneuvering and the video processor is plagued with such difficulties as measurement noise, false targets, and fading problems. In a more general sense one hopes to learn what information is required from the radar to track adequately.

Section 2.0 investigates the relationship between the characteristics of maneuvering targets and the signals as seen by the radar. Section 3.0 studies the errors associated with α-β trackers caused by maneuvering targets and the measurement noise. In addition the probability of breaking track is discussed. Sections 4.0 and 5.0 investigate the performance limitations due to false targets and fades, respectively. A discussion of the results is given in Section 6.0.

2.0 TRANSLATION OF TARGET CHARACTERISTICS INTO RADAR REQUIREMENTS

In describing the performance or design of any system, it is important to know the characteristics of the signals which excite the system. The discussion given below is concerned with the problem of obtaining these characteristics.

In examining target trajectories one finds that there exists an uncountable number of possible trajectories and that they are random in character. Although in theory each trajectory could be used individually to investigate the system performance, it does become difficult, due to the vast number of trajectories, to assimilate and use the large amount of information. The two procedures that are usually used to circumvent this problem are as follows. The first procedure is concerned with constructing a probabilistic description of the trajectories and the second procedure is concerned with the construction of a small set of trajectories which are typical in their frequency content. The latter of these two approaches is considered in this section.

The discussion begins by making the following a priori assumption: All target trajectories can be approximated by either straight-line, constant-altitude trajectories, constant-g turns, or changes in altitude associated with the previous two maneuvers over at least a segment of the trajectory. The number of trajectories is further limited due to the physical laws the target must obey according to its design. In the case of aircraft, these limitations can be characterized in terms of velocity, acceleration, and structural loading g. As a last consideration the target performance must be translated into signals that the radar measures, which are range and azimuth. The limited set of trajectories described above is now analyzed.

2.1 Straight-Line, Constant-Altitude Targets

The geometry of the target trajectory is shown in Fig. 2.1, where x and y are the rectangular coordinates, r and θ the range and azimuth, and ϕ, v, and a are the heading, velocity, and acceleration of the target, respectively.

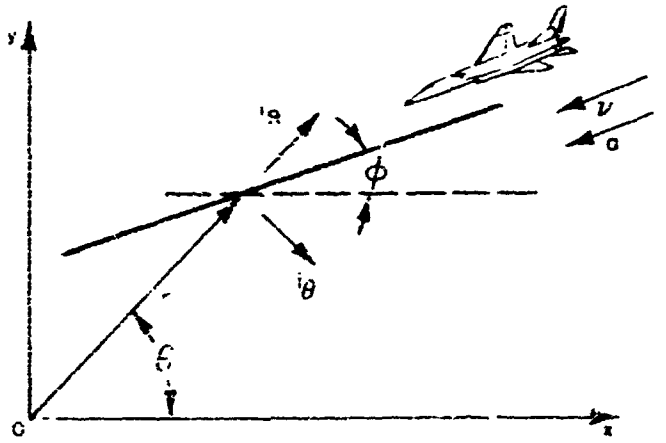

Fig. 2.1—Geometry of a straight-line, constant altitude target

The following quantities are defined.

$$r = \sqrt{x^2 + y^2} \tag{2.1}$$

$$\theta = \tan^{-1} \frac{y}{x} \tag{2.2}$$

$$v_x = v \cos \phi \tag{2.3}$$

$$v_y = v \sin \phi . \tag{2.4}$$

Taking the derivatives of Eqs. (2.1) and (2.2) and using Eqs. (2.3) and (2.4) yield the range and azimuth velocities

$$v_R = v \cos (\theta - \phi) \tag{2.5}$$

and

$$v_\theta = -\frac{v}{r} \sin (\theta - \phi) . \tag{2.6}$$

Taking the second derivatives gives the range and azimuth accelerations

$$a_R = \frac{v^2}{r} \sin^2 (\theta - \phi) + a \cos (\theta - \phi) \tag{2.7}$$

$$a_\theta = \frac{a}{r} \sin (\theta - \phi) + 2 \frac{v^2}{r^2} \sin (\theta - \phi) \cos (\theta - \phi) . \tag{2.8}$$

If one computes the total acceleration a_T of the target, one finds

$$a_T = (a_R - r v_\theta^2) i_R + (r a_\theta + 2 v_R v_\theta) i_\theta . \tag{2.9}$$

Substituting Eqs. (2.5) through (2.8) into Eq. (2.9) yields

$$a_T = a \cos (\theta - \phi) i_R + a \sin (\theta - \phi) i_\theta . \tag{2.10}$$

The magnitude of a_T is

$$|a_T| = a . \tag{2.11}$$

It is interesting to note that the range and azimuth accelerations as seen by the radar can be quite different from the acceleration of the target. In fact the radar sees an acceleration just due to the motion of the target. The effect of this apparent acceleration is next investigated.

The maximum magnitude of the range or azimuth acceleration is proportional to

$$a_{max} = \frac{v^2}{r} \tag{2.12}$$

and the g_N of the turn is defined to be

$$g_N = \frac{a_{max}}{g} , \tag{2.13}$$

where g is the gravitational constant.

The effect of this acceleration is shown in Fig. 2.2. This curve shows that at the near ranges these apparent accelerations could be troublesome. However, most search radars are not concerned with such short ranges, and these effects can usually be ignored. In summary, for the far regions one finds that the range acceleration depends only on the target's acceleration and on its angle with respect to the radar. The azimuth acceleration, in addition to depending on these quantities, also depends upon range.

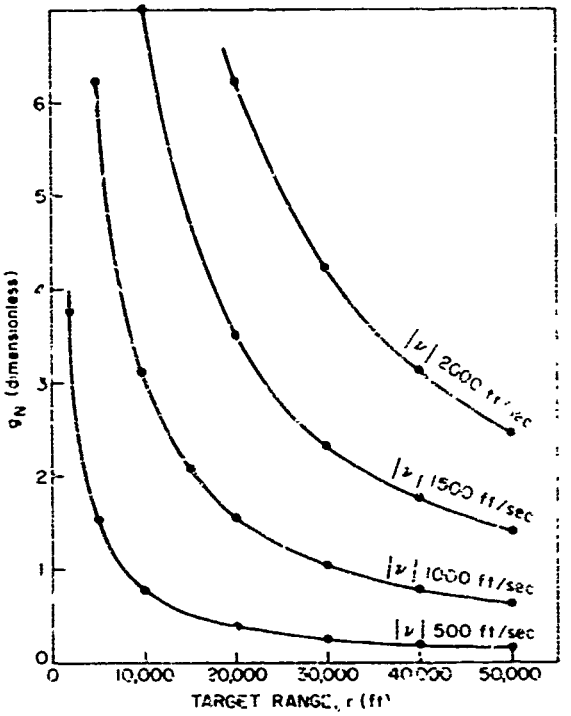

Fig. 2.2—Range acceleration at close ranges for straight-line, constant-altitude, and velocity target trajectories

2.2 Turn Analysis in Terms of Circular Motion

A target moving in a circular path with a constant velocity is used to approximate a turn. The geometry is shown in Fig. 2.3.

The law of cosines for the triangle is written

$$r^2 = \rho^2 - R^2 - 2\rho R \cos\phi \tag{2.14}$$

and can be rewritten as

$$\frac{r}{\sqrt{\rho^2 + R^2}} = \sqrt{1 - \frac{2\rho R}{(\rho^2 + R^2)} \cos\phi} \ . \tag{2.15}$$

Recall the following expansion,

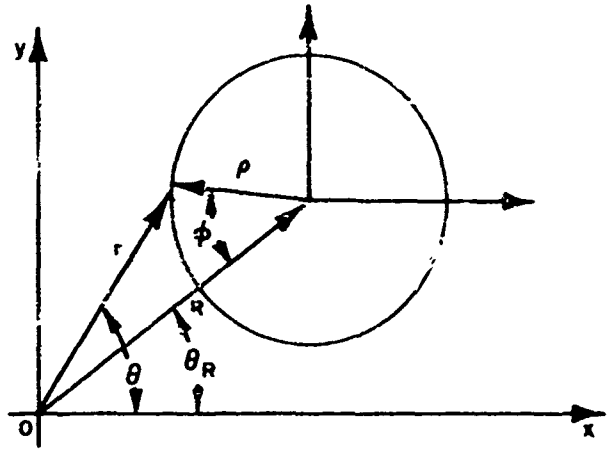

Fig. 2.3—Geometry of a constant-g turn

$$\sqrt{1-x} = 1 - \frac{x}{2} - \frac{1}{2}\cdot\frac{1}{4}x^2 - \frac{1}{2}\cdot\frac{1}{4}\cdot\frac{3}{6}x^3 + \underline{0} \tag{2.16}$$

where

$$x^2 \leqslant 1 .$$

Using the series expansion Eq. (2.15) is written as

$$r = \sqrt{\rho^2 + R^2} - \frac{\rho R}{\sqrt{\rho^2 + R^2}} \cos\phi - \frac{1}{2}\frac{\rho^2 R^2}{\sqrt[3]{\rho^2 + R^2}} \cos^2\phi$$

$$- \frac{1}{2}\frac{\rho^3 R^3}{\sqrt[5]{\rho^2 + R^2}} \cos^3\phi - \underline{0} \tag{2.17}$$

For $\rho \ll R$, Eq. (2.17) can be approximated as

$$r \approx R - \rho\cos(\dot{\phi}t) \tag{2.18}$$

where

$$\dot{\phi} = \left(\frac{\phi}{t}\right).$$

The range is found to vary in a sinusoidal manner. In addition R must be reasonably large. To show that this condition must also be satisfied such that Eq. (2.18) is valid, one only needs to differentiate Eq. (2.17) twice to find the range acceleration a_R. First noting that

$$\dot{\phi} = \frac{v}{\rho} , \tag{2.19}$$

the range acceleration becomes

$$a_R = \frac{v^2}{\rho} \sin\phi + \frac{v^2}{2R} \cos 2\phi + \underline{0} \,. \tag{2.20}$$

for $\rho \ll R$.

In observing Eq. (2.20) one finds the same troublesome apparent accelerations as found for the constant-altitude, straight-line target trajectories. Even though the amplitude of the harmonies in range can be rather small at close ranges, the acceleration of the target as seen by the radar can be quite large over at least a short interval of time. This effect is similar to a harmonic approximation of a square wave. Considering the first few harmonics which are all reasonably small compared to the fundamental one, we see that rapid changes in slope can occur over small intervals of time.

The analysis of the azimuth measurement for a target moving in a circle closely parallels the range measurement analysis. One begins by writing the law of sines for the triangle shown in Fig. 2.3,

$$\frac{\sin(\theta - \theta_R)}{\rho} = \frac{\sin\phi}{r} \,. \tag{2.21}$$

Solving for θ, one finds

$$\theta = \theta_R + \sin^{-1}\left(\frac{\rho}{r} \sin\phi\right) . \tag{2.22}$$

Expansion into a series yields

$$\theta = \theta_R + \frac{\rho}{r} \sin\phi - \left(\frac{\rho}{r}\right)^3 \sin^3\phi + \underline{0} \,. \tag{2.23}$$

For the case $\rho/r \ll 1$, Eq. (2.18) can be substituted into Eq. (2.23), yielding

$$\theta = \theta_R + \frac{\rho \sin\phi}{R - \rho\cos\phi} + \underline{0} \,. \tag{2.24}$$

Using a division process, Eq. (2.24) can be rewritten as

$$\theta = \theta_R + \frac{\rho}{R} \sin\dot{\theta}t + \frac{\rho^2}{2R^2} \sin 2\dot{\theta}t + \underline{0} \,. \tag{2.25}$$

The azimuth acceleration is computed to be

$$a_\theta = -\frac{1}{R}\left(\frac{v^2}{\rho}\right) \sin\dot{\theta}t - \frac{2}{R}\left(\frac{v^2}{R}\right) \sin 2\dot{\theta}t + \underline{0} \,. \tag{2.26}$$

Again one finds that if $\rho \ll R$ and if R is large, the azimuth variation is nearly a sinusoid. If these conditions are not met, the harmonics can cause a considerable azimuth deviation over a small interval of time.

It is instructive to show an example of the range and azimuth measurements and their derivatives for a circular-motion target for two different ranges. The target was moved in

a circle at a constant altitude of 1009 ft, the center of curvature was located at an azimuth of 45°, and ranges of 14,140 ft or 141,400 ft were used. The target velocity was 1200 ft/sec and the g_N of the turn was 6. The range and azimuth variations with their derivatives are shown in Figs. 2.4 and 2.5. Observing these curves one finds that at the large ranges the variations are nearly sinusoidal. At the shorter distances it is found that the signals are rich in harmonics and large accelerations can result. In addition it is found that the azimuth variations are quite small for the far ranges in comparison to the near ones.

2.3 Accelerating, Circular-Motion Targets

It is first assumed that the target is operting in the far region such that the range and azimuth variations can be assumed to be sinusoids. The target is assumed to be moving in a circular path except that now it may have a tangential component of acceleration. This tangential acceleration is expressed in terms of angular acceleration, and is assumed to be sinusoidal; i.e.,

$$a_\theta = \frac{a}{\rho} \sin \omega_m t \,. \tag{2.27}$$

Integrating twice to find the phase, it is then placed into Eq. (2.18), yielding

$$r = R + \rho \cos \left(\omega_0 t + \frac{a}{\rho \omega_m^2} \sin \omega_m t \right) , \tag{2.28}$$

where

$$\omega_0 = \dot{\phi} = \frac{v}{\rho} \,.$$

A well-known Fourier series expansion exists for this waveform in terms of Bessel functions (1):

$$r = R + \rho J_0 \left(\frac{a}{\rho \omega_m^2} \right) \cos \omega_0 t + 2\rho J_2 \left(\frac{a}{\rho \omega_m^2} \right) \cos \; 2(\omega_0 - \omega_m)t$$

$$- 2\rho J_2 \left(\frac{a}{\rho \omega_m^2} \right) \cos \; 2(\omega_0 + \omega_m)t \; + \; \underline{0} \,. \tag{2.29}$$

As the tangential acceleration goes to zero, Eq. (2.29) reduces to that of the constant-velocity, circular-motion target

$$r = R + \rho \cos \omega_0 t \,. \tag{2.30}$$

The tangential acceleration in a turn has the effect of spreading the frequency spectra. The above analysis is only valid for small values of $(a/\rho \omega_m^2)$ because of physical considerations.

It is probably worthwhile commenting on targets changing altitude. If one allows no azimuth changes, the analysis so far applies to this problem by merely exchanging the word elevation for azimuth. An analysis of target characteristics considering all three measurements is not attempted.

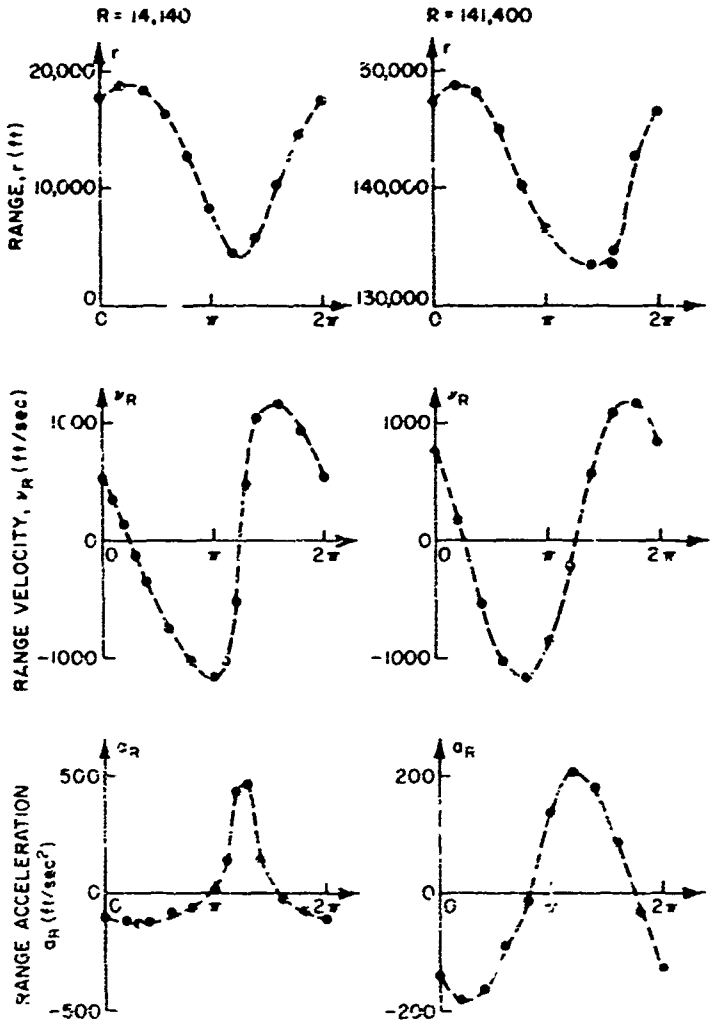

Fig. 2.4—Comparison of range and derivatives for circular-motion targets at two ranges

2.4 Frequency Response Characteristics

The discussion is begun by considering only constant-velocity, circular-motion targets. In these cases only the fundamental sinusoid is present. Thus

$$r = R - \rho \cos \dot{\phi} t \tag{2.31}$$

$$\theta = \theta_R + \frac{\rho}{R} \sin \dot{\phi} t \tag{2.32}$$

$$\dot{\phi} = \frac{v}{\rho} \tag{2.33}$$

$$\rho = \frac{v^2}{gEN} . \tag{2.34}$$

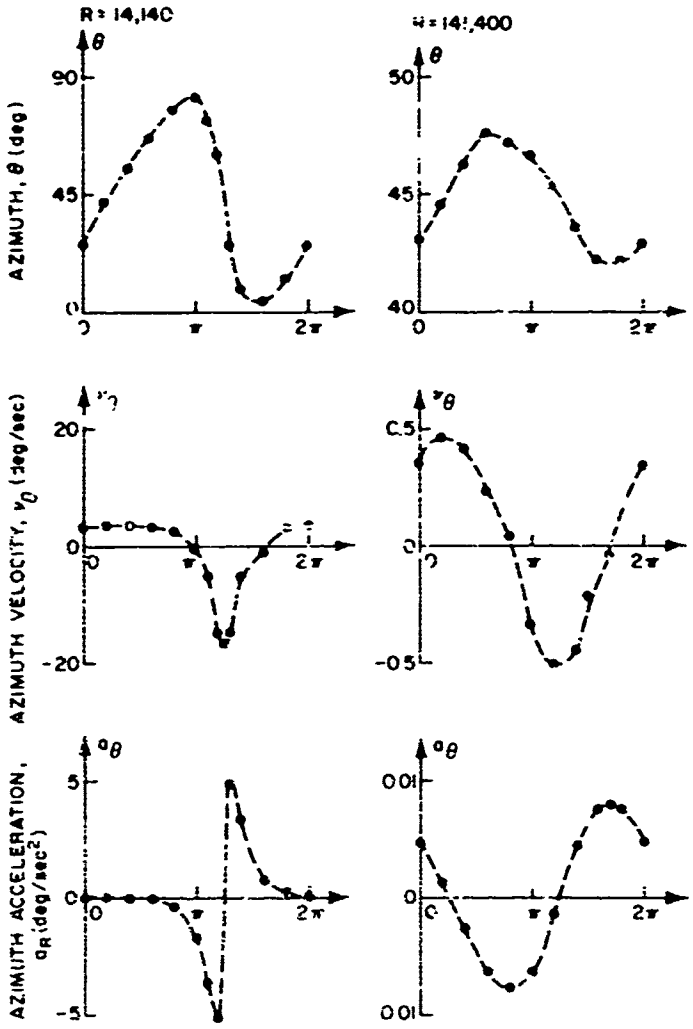

Fig. 2.5—Comparison of azimuth and derivatives for circular-motion targets at two ranges

Substituting Eq. (2.34) into (2.31), (2.32), and (2.33), one obtains

$$r = R - \frac{v^2}{gg_N} \cos\left(\frac{gg_N}{v}\, t\right) \tag{2.35}$$

$$\theta = \theta_R + \left(\frac{v^2}{Rgg_N}\right) \sin\left(\frac{gg_N}{v}\, t\right) . \tag{2.36}$$

Observing Eqs. (2.35) and (2.36) one finds that the amplitude frequency characteristics of range depend only on the aircraft parameters of the structural loading g and velocity. The azimuth in addition depends on range. The amplitude is plotted vs frequency for various velocities and for sharpness of the turn indicated by g_N in Fig. 2.6. One finds that as g_N for fixed v is increased, the amplitude decreases and the frequency increases. As the velocity for fixed g_N is increased, the amplitude increases and frequency decreases.

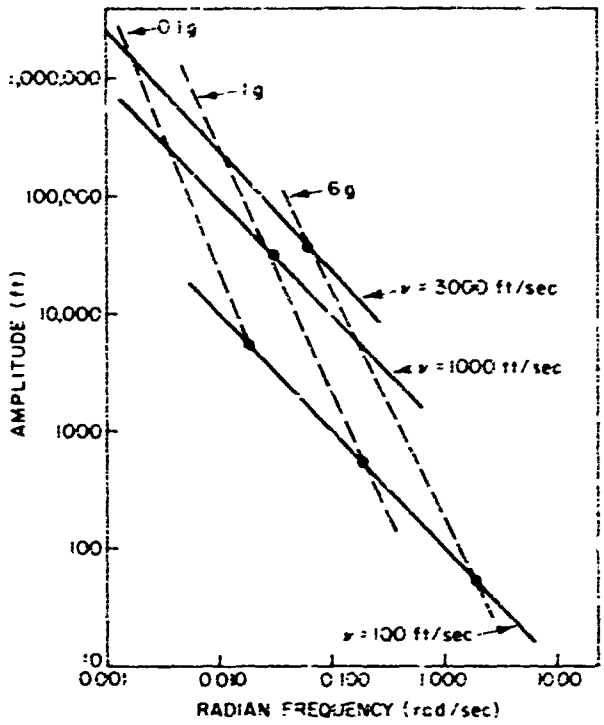

Fig. 2.6—Amplitude vs frequency plot for a circular-motion target

An example of the trajectory of a high-performance aircraft performing "dogfight" type maneuvers is given in Fig. 2.7. The range and azimuth variations with time are given in Figs. 2.8 and 2.9 for this maneuver. This example again shows that the frequencies encountered in even high-performance targets are quite low.

2.5 Discussion of Results

The purpose of this section is to translate the target characteristics into signals on which the radar must track. It was found that the three target parameters g, v, and a can be used to characterize the limitations on the received signals in terms of amplitude and frequency characteristics. If the near effects could be ignored, the signals set up by the target were found to be quite low in frequency; typical values may be in the order of 0.2 Hz or lower. However, if the target has a tangential component of acceleration as well as a turning motion, higher harmonics in the radar signal may be observed in which the highest significant observable frequency may be 0.6 to 0.8 Hz.

It is assumed throughout the remainder of this discussion that only the polar coordinate system will be used for tracking and that the near effects for all practical purposes can be ignored.

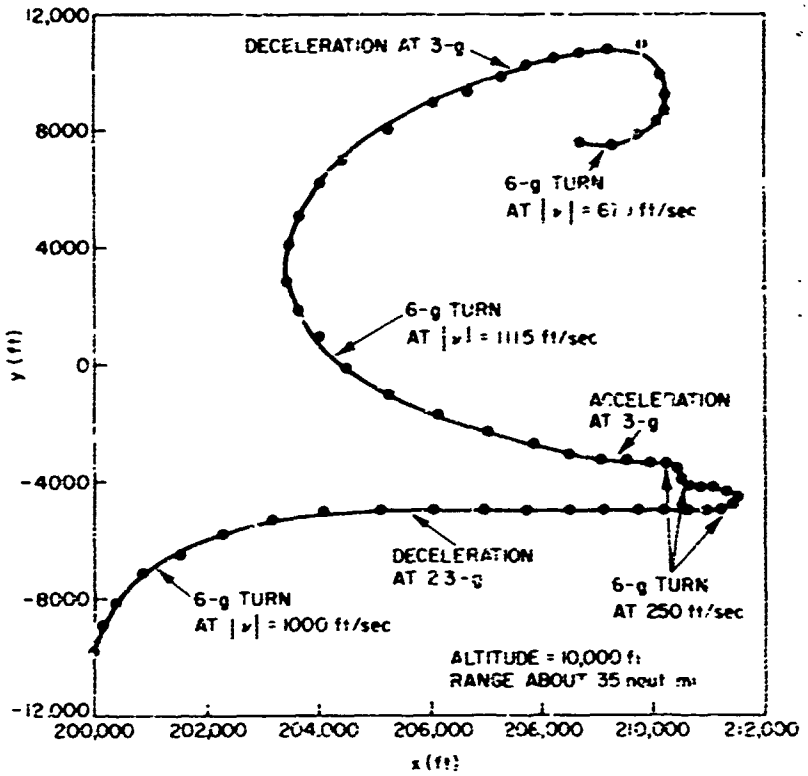

Fig. 2.7—Highly maneuverable target trajectory of a shown in xy coordinates

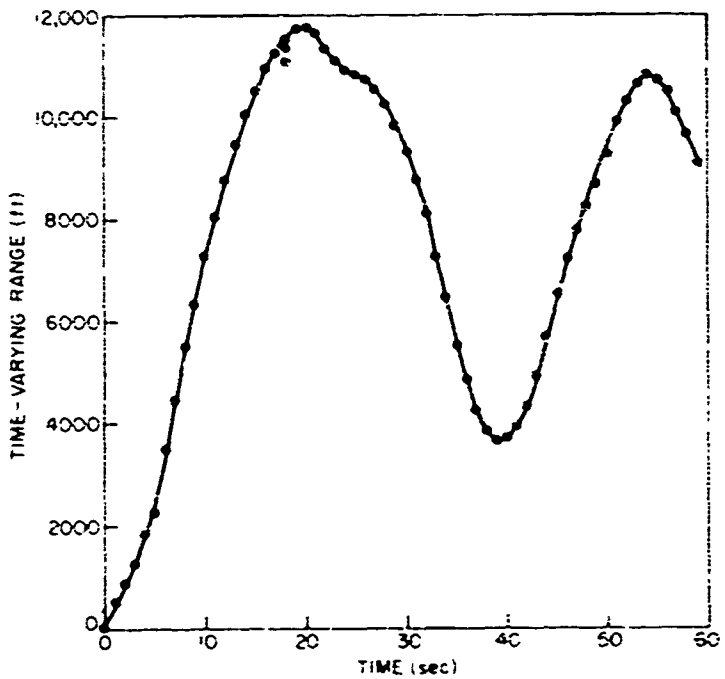

Fig. 2.8—Time history of range for a target performing maneuvers in a limited space, range about 35 naut. mi.

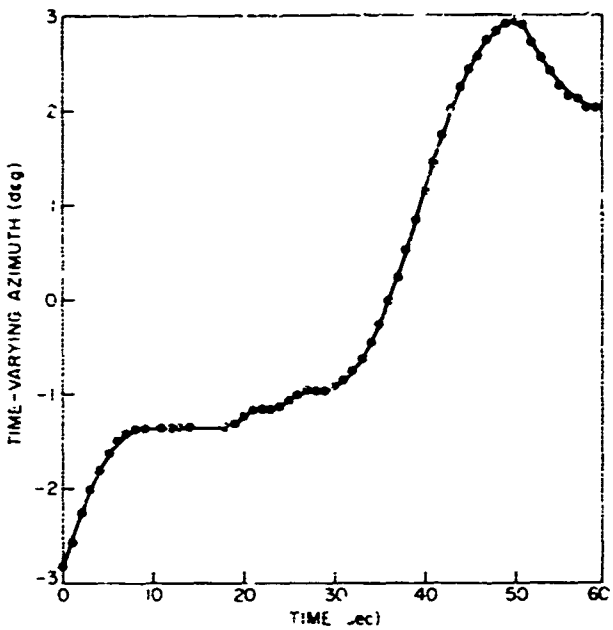

Fig. 2.9—Time history of azimuth for a target maneuvering in a limited space; range about 35 naut. mi.

3.0 OPERATION OF TRACKING EQUATIONS EXCLUDING FALSE TARGET AND FADING CONDITIONS

In general the tracking equations must perform three functions. They must compute the velocity, smooth both the measured position and computed velocity, and finally predict a new coordinate on which to center the correlation region. The α-β tracking equations are first defined and the errors in both the mean and variance of the predicted coordinates are investigated. Finally the probability of breaking track is discussed.

3.1 Definition of Tracking Equations

The well-known α-β tracking equations are defined as

$$X_p^N = X_s^{N-1} + V_s^{N-1}T \tag{3.1}$$

$$X_s^N = X_p^N + \alpha(X_m^N - X_p^N) \tag{3.2}$$

$$V_s^N = V_s^{N-1} + \frac{\beta(X_m^N - X_p^N)}{T} \tag{3.3}$$

where

X_p = predicted position
X_s = smoothed position
V_s = smoothed velocity
X_m = measured position
α, β = filter parameters
T = sampling time

For purposes of analysis, these equations are more usable if one substitutes Eq. (3.1) into Eqs. (3.2) and (3.3), yielding

$$\begin{bmatrix} X_s \\ V_s \end{bmatrix}^N = \begin{bmatrix} (1-\alpha) & (1-\alpha)T \\ -\beta/T & (1-\beta) \end{bmatrix} \begin{bmatrix} X_s \\ V_s \end{bmatrix}^{N-1} + \begin{bmatrix} \alpha \\ \beta/T \end{bmatrix} [X_m]^N \tag{3.4}$$

and

$$[X_p]^{N+1} = [1 \quad T] \begin{bmatrix} X_s \\ V_s \end{bmatrix}^N . \tag{3.5}$$

For convenience, Eqs. (3.4) and (3.5) are put in block diagram form in Fig. 3.1 and the following matrixes and vectors are defined:

$$\mathbf{A} = \begin{bmatrix} (1-\alpha) & (1-\alpha)T \\ -\beta/T & (1-\beta) \end{bmatrix}$$

$$\mathbf{B} = \begin{bmatrix} \alpha \\ \beta/T \end{bmatrix}$$

$$\mathbf{C} = [1 \quad T]$$

$$\mathbf{X} = \begin{bmatrix} X_s \\ V_s \end{bmatrix}.$$

At this point the system has been reduced into a more tractable form for analysis.

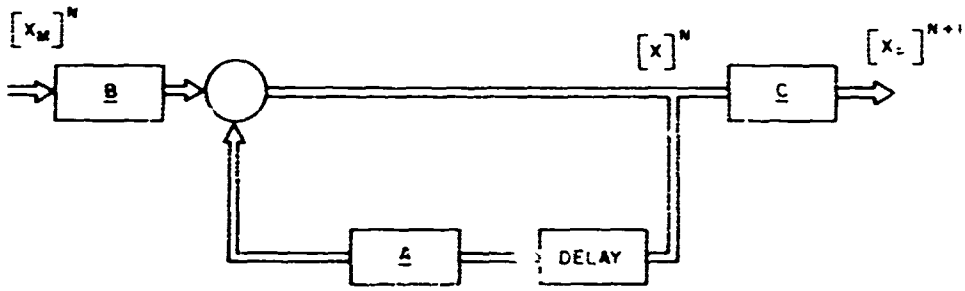

Fig. 3.1—Block diagram of an α-β tracker

3.2 Stability Analysis

Since the system is in the form of difference equations, it is proposed to investigate the stability through the use of the Z-transform (2). Taking the Z-transform of Eq. (3.4) results in

$$\mathbf{X}(Z) = \mathbf{A}Z^{-1}\,\mathbf{X}(Z) + \mathbf{B}X_m(Z). \tag{3.6}$$

The system transfer function is defined as

$$G(Z) = \frac{X(Z)}{X_m(Z)} = [I - AZ^{-1}]^{-1}B . \tag{3.7}$$

For the specific system in question, Eq. (3.7) becomes

$$G_x(Z) = \frac{X_s(Z)}{X_m(Z)} = \frac{\alpha Z\left(Z + \frac{\beta - \alpha}{\alpha}\right)}{Z^2 \text{ Det } [I - AZ^{-1}]^{-1}} \tag{3.8}$$

$$G_v(Z) = \frac{V_s(Z)}{X_m(Z)} = \frac{\frac{\beta}{T} Z(Z-1)}{Z^2 \text{ Det } [I - AZ^{-1}]^{-1}} , \tag{3.9}$$

where

$$Z^2 \text{ Det } [I - AZ^{-1}] = Z^2 - Z(2 - \alpha - \beta) + (1 - \alpha) . \tag{3.10}$$

The stability of the system depends on the case for which at least one root of the Z^2 Det $[I - AZ^{-1}]$ lies outside the unit circle. Several typical root loci are shown in Figs. 3.2 and 3.3. As can be seen, the parameter α seems to control the radius of the loci and β controls the amount the pole has moved. For cases in which $\alpha > 1$, the loci never leaves the real axis. The stability criterion can be found by setting the most negative root equal to -1,

$$Z = -1 = \frac{(2 - \alpha - \beta)}{2} - \frac{1}{2}\sqrt{(\alpha + \beta)^2 - 4\beta} . \tag{3.11}$$

Solving, one finds that

$$\beta \leq 4 - 2\alpha . \tag{3.12}$$

In addition to the stability criterion, a zero in Eq. (3.7) can lie outside the unit circle. This situation will not be allowed since it usually leads to undesirable system response (2). The condition one must satisfy is

$$\beta \leq 2\alpha . \tag{3.13}$$

The permissible values of α and β are shown in Fig. 3.4. Further restrictions will be placed on this region later.

3.3 Frequency Response Characteristics

The frequency response of the filter can be found by placing $Z = e^{j\omega T}$ into Eqs. (3.8) and (3.9). The magnitude and phase characteristics of $G_x(Z)$ and $G_v(Z)$ are shown in Figs. 3.5, 3.6, and 3.7.

Observing these figures one finds that α should never be larger than one. For $\alpha < 1$, α seems to control the bandwidth of the low-pass filter and β has more control over the

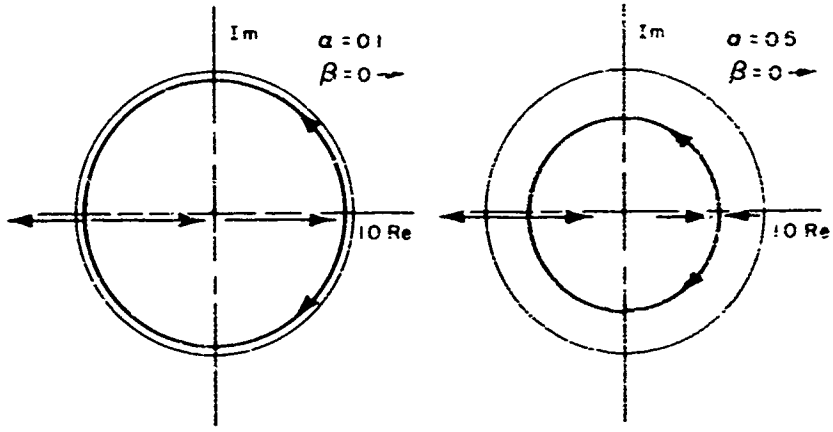

Fig. 3.2—Root loci of α-β tracker transfer functions

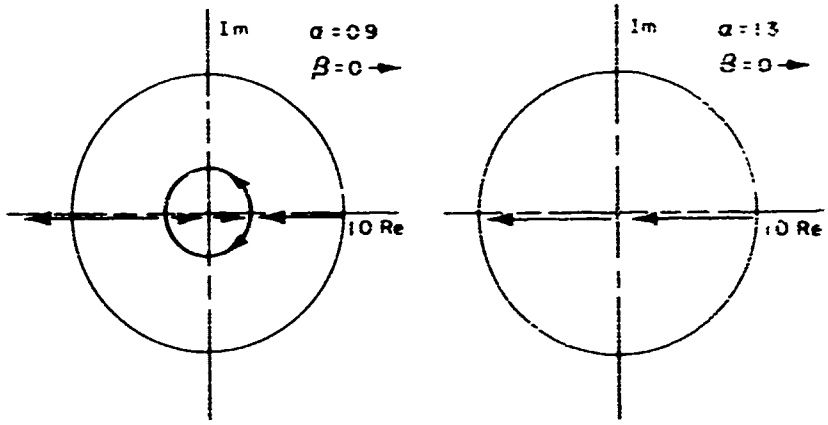

Fig. 3.3—Root loci of α-β tracker transfer functions

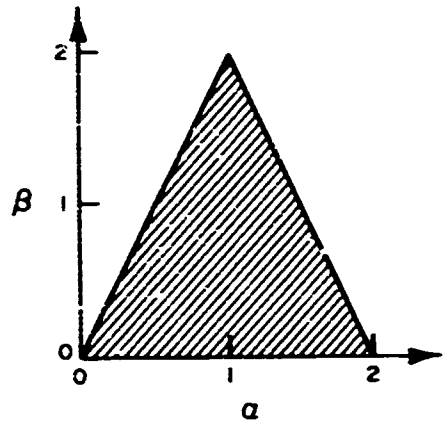

Fig. 3.4—Allowable values of α and β in α-β tracker

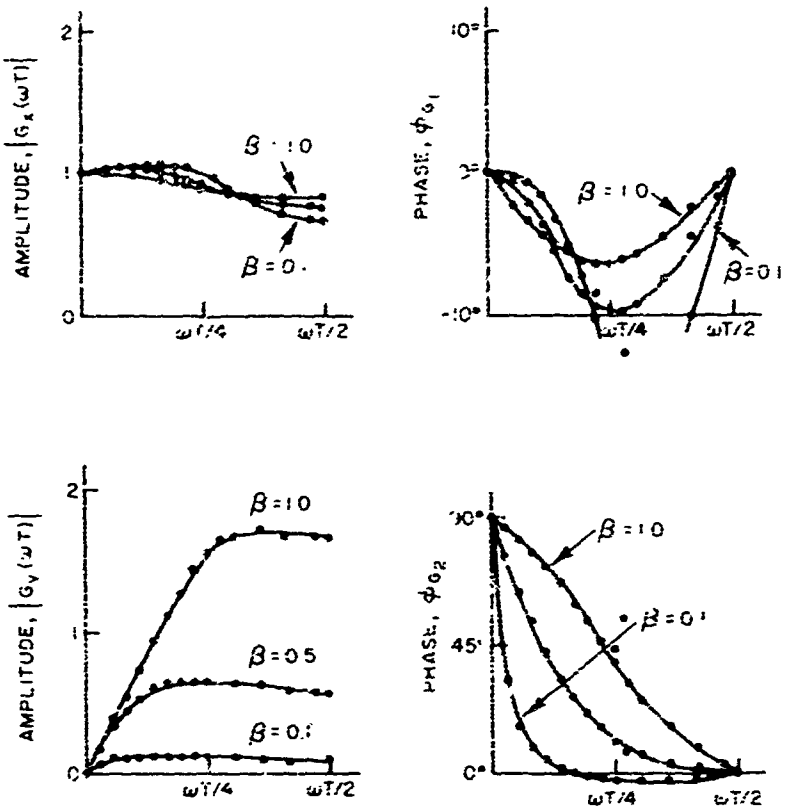

Fig. 3.5—Amplitude and phase characteristics of the tracking equations for $\alpha = 0.9$

damping. In fact β should be somewhat smaller than α such that resonant spikes do not occur. Observing Fig. 3.5, one finds that the measured position is nearly unsmoothed and that $G_v(Z)$ is in the form of a differentiator. In general α and β should be set such that $G_x(Z)$ passes the highest expected frequency undistorted, and $G_v(Z)$ acts as a good differentiator up to the highest expected frequency.

3.4 Noise Characteristics of Filter

The discussion is begun by making the following change of variable:

$$\Delta X = V_s T. \tag{3.14}$$

Equations (3.4) and (3.5) describing the filter can be rewritten as

$$\begin{bmatrix} X_s \\ \Delta X \end{bmatrix}^N = \begin{bmatrix} (1-\alpha) & (1-\alpha) \\ -\beta & (1-\beta) \end{bmatrix} \begin{bmatrix} X_s \\ \Delta X \end{bmatrix}^{N-1} + \begin{bmatrix} \alpha \\ \beta \end{bmatrix} [X_m]^N \tag{3.15}$$

$$[X_p]^{N+1} = \begin{bmatrix} 1 & 1 \end{bmatrix} \begin{bmatrix} X_s \\ \Delta X \end{bmatrix}^N, \tag{3.16}$$

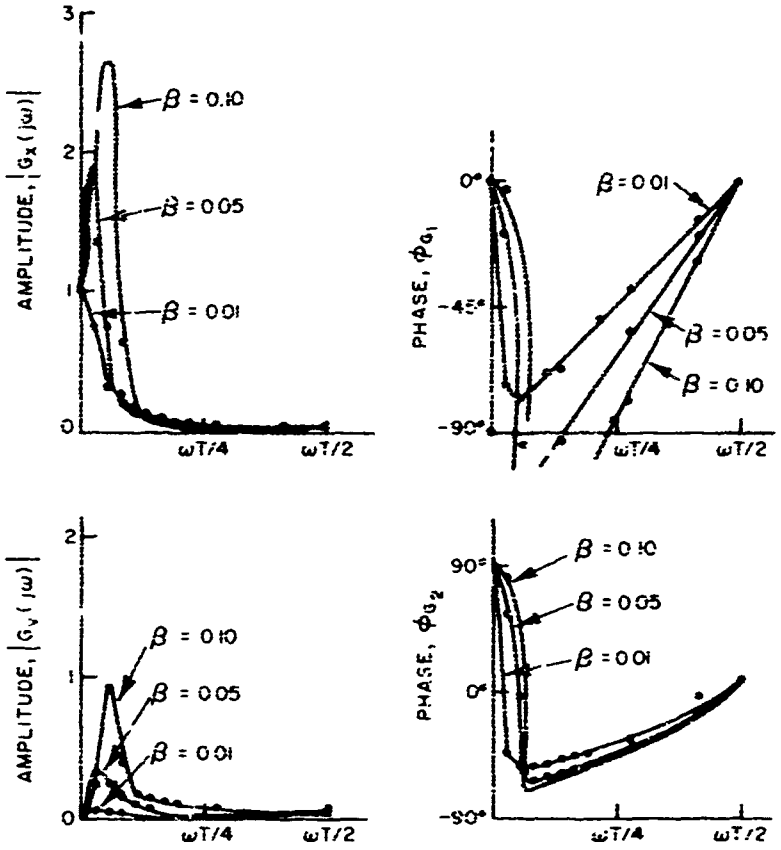

Fig. 3.6—Amplitude and phase characteristics of tracking equations for $\sigma = 0.1$

where now

$$\mathbf{A}' = \begin{bmatrix} (1-\alpha) & (1-\alpha) \\ -\beta & (1-\beta) \end{bmatrix}$$

$$\mathbf{B}' = \begin{bmatrix} \alpha \\ \beta \end{bmatrix}$$

$$\mathbf{C}' = \begin{bmatrix} 1 & 1 \end{bmatrix}$$

The mean and covariance equations are defined as (3)

$$[\overline{X}]^N = \mathbf{A}'\overline{\mathbf{X}}^{N-1} + B'\overline{\mathbf{X}}_m^N \tag{3.17}$$

$$\mathbf{P}^N = \mathbf{A}'\mathbf{P}^{N-1}\mathbf{A}'^T + \mathbf{B}'\sigma^2 B'^T \tag{3.18}$$

where $[\overline{X}]^N = E[\mathbf{X}^N]$, the expected value.

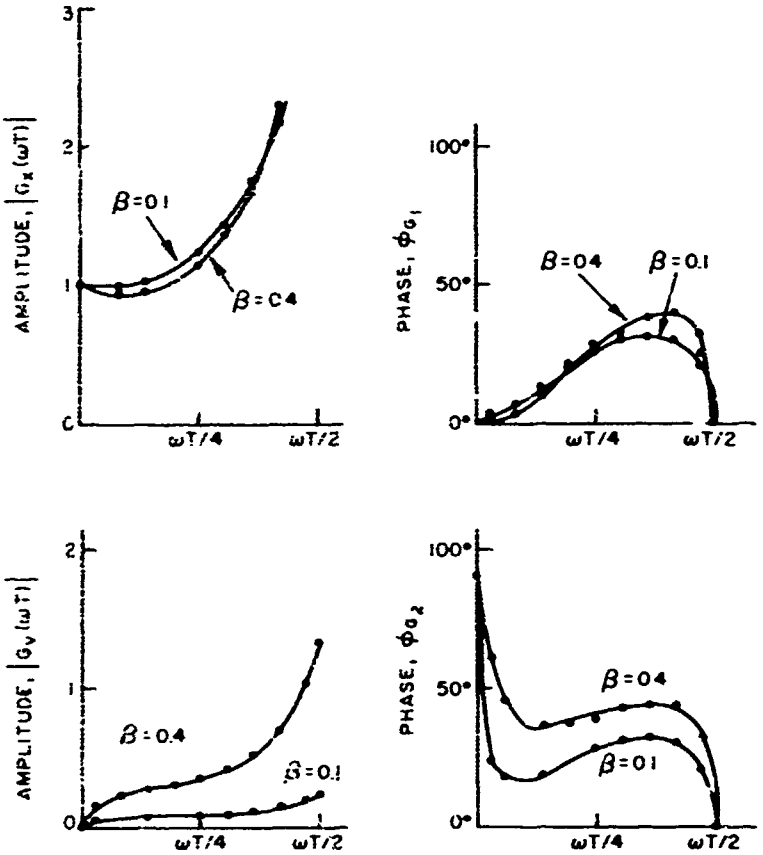

Fig. 3.7—Amplitude and phase characteristics of the tracking equations for $\alpha = 1.5$

$$P = \begin{bmatrix} P_{11} & P_{12} \\ P_{21} & P_{22} \end{bmatrix}$$

$$P_{11} = E\left[(X_s - \bar{X}_s)(X_s - \bar{X}_s)\right]$$

$$P_{12} = E\left[(X_s - \bar{X}_s)(\Delta X - \Delta \bar{X})\right] = P_{21}$$

$$P_{22} = E\left[(\Delta X - \Delta \bar{X})(\Delta X - \Delta \bar{X})\right]$$

σ_{xm} = standard deviation of measurement error .

The mean equations are just the response of the system to a deterministic input which will be studied later. The covariance equation becomes

$$\begin{bmatrix} P_{11} \\ P_{12} \\ P_{22} \end{bmatrix}^N = \begin{bmatrix} (1-\alpha)^2 & 2(1-\alpha)^2 & (1-\alpha)^2 \\ -\beta(1-\alpha) & (1-2\beta)(1-\alpha) & (1-\beta)(1-\alpha) \\ \beta^2 & -2\beta(1-\beta) & (1-\beta)^2 \end{bmatrix} \begin{bmatrix} P_{11} \\ P_{12} \\ P_{22} \end{bmatrix}^{N-1} + \begin{bmatrix} \alpha^2 \\ \alpha\beta \\ \beta^2 \end{bmatrix} \sigma_{X_m}^2 \quad (3.19)$$

The variance of the predicted position is easily computed in terms of the variances given in Eq. (3.19):

$$\sigma^2_{X_p} = P_{11} + 2P_{12} + P_{22} . \tag{3.20}$$

Ignoring the transients during the time the track is being established, the steady state solution is found by recursively solving Eq. (3.19). The predicted noise power is normalized,

$$\sigma_0^2 = \frac{\sigma^2_{X_p}}{\sigma^2_{X_m}} , \tag{3.21}$$

and plotted as a function of α and β in Fig. 3.8. Observing Fig. 3.8 one finds that the input noise power can be reduced or filtered if α and β are appropriately adjusted. One also finds that the parameter β greatly affects the predicted noise power. This effect should be expected since differentiated noise is quite noisy and β affects this quantity. In fact the variance of the predicted position can be larger than the input noise because of differentiation.

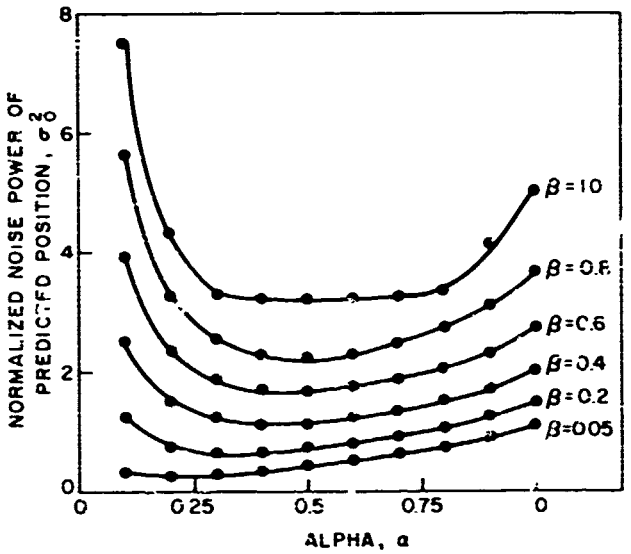

Fig. 3.8– Predicted position noise power as a function of α,β

An interesting phenemenon occurs for small values of α and large values of β. The noise power increases sharply. The reason for this may most easily be seen by looking at the frequency responses in Fig. 3.6. The large resonant peaks in the response allow a lot of noise to come through. In addition a non-minimal phase condition can be reached and the noise then increases rapidly.

The noise power is not a function of the sampling time. As the sampling time decreases the variance of the velocity increases; however, this effect is canceled out by having to predict over a shorter interval of time.

3.5 Deterministic Error Analysis

Various sinusoidal waveforms are passed through the filter and the root mean square error σ between the predicted and true positions is

$$\sigma = \sqrt{\frac{1}{N}\sum_{i=1}^{N}(X_p^i - X_m^i)^2}\ , \tag{3.22}$$

where

$$X_p^i = |G_x(j\omega)| \sin(i\omega T + \phi_{G_x}) + |G_v(j\omega)| \sin(i\omega T + \phi_{G_v})\ ,$$

given that

$$X_m^i = \sin\left((i+1)\omega T\right)\ .$$

(the amplitude of the sinusoid equals one for normalization)

The rms error is plotted vs the ratio of the frequency f of the sinusoid f to the sampling frequency f_T for various values of α and β in Figs. 3.9 through 3.11.

Upon inspecting these curves one finds that if either the waveform is sampled faster or the frequency of the waveform is lessened, then the error decreases. In addition the lightly filtered systems have fewer errors in the means than the heavily filtered systems. The regions of the curves where the error is near unity only indicate that one is not sampling at a sufficient rate.

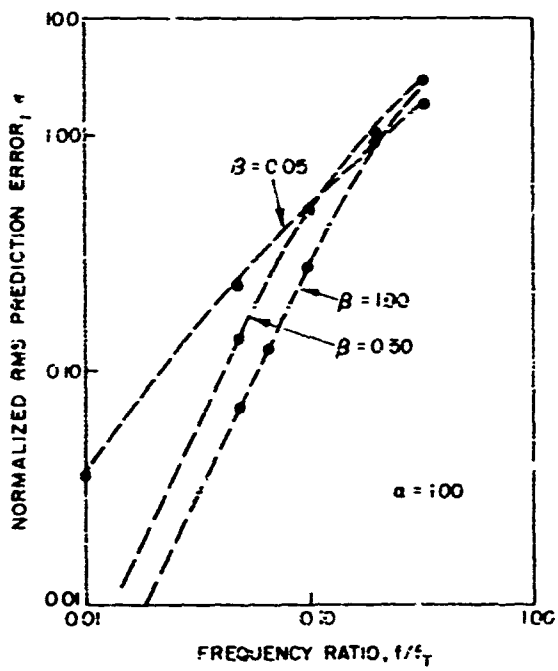

Fig. 3.9—Deterministic prediction error as a function of f/f_T, α, β

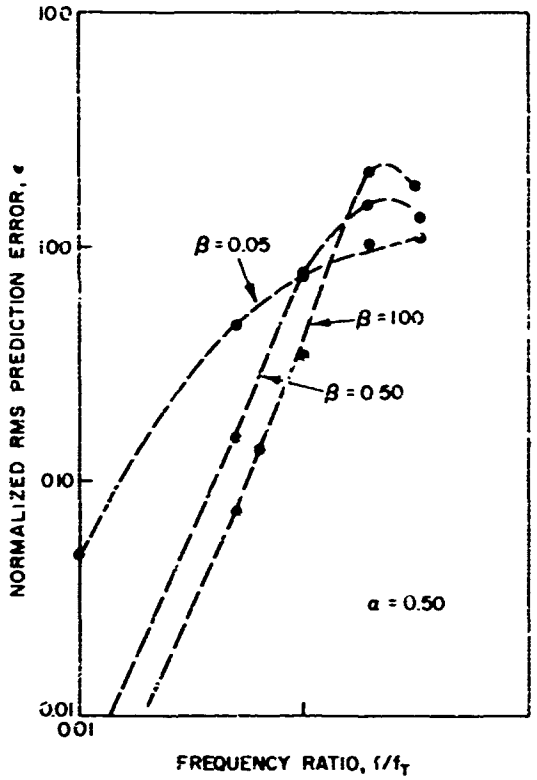

Fig. 3.10—Deterministic prediction error as a function of f/f_T, α, β

3.f Probability of Breaking Track

A correlation region, as shown in Fig. 3.12, is defined to be a region of space centered about the predicted value. If $|X_m - X_p| < \gamma$, then the measured value is said to lie in the correlation region.

The random variables X_m and X_p are gaussian-distributed random variables as shown in Fig. 3.13. The random variable ω is defined as

$$\omega = X_m - X_p \, . \tag{3.23}$$

Since X_p and X_m are gaussian, ω is also gaussian. The mean and variance of ω are

$$\overline{\omega} = \overline{X}_m - \overline{X}_p \tag{3.24}$$

$$\sigma_\omega^2 = \sigma_{X_p}^2 + \sigma_{X_m}^2 \, . \tag{3.25}$$

The probability of breaking track* at a particular sample instance is defined as the probability that $|X_m - X_p| > \gamma$.

*This assumes that once the target is outside the correlation region it will remain outside of it for all time.

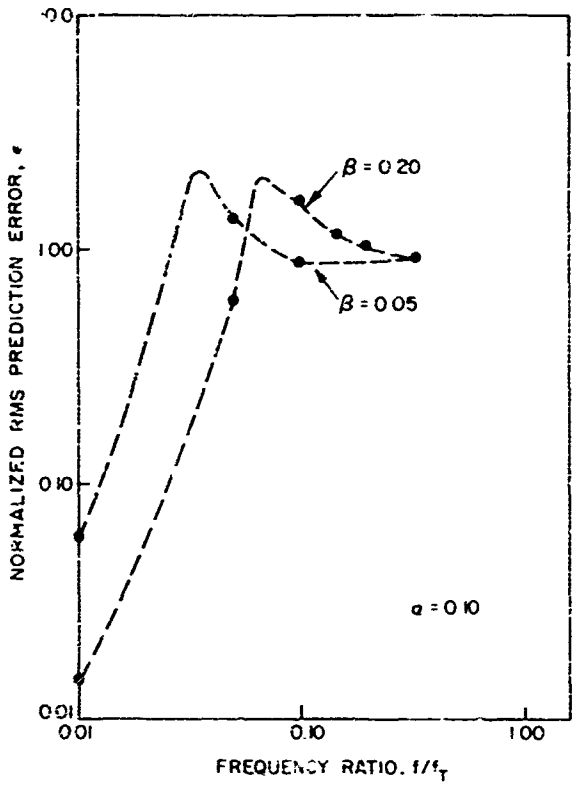

Fig. 3.11—Deterministic prediction error as a function of f/f_T, α, β

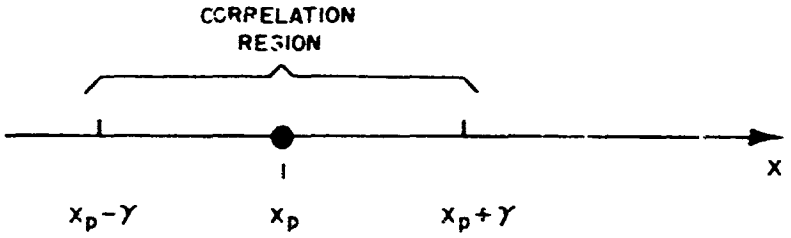

Fig. 3.12—Correlation region

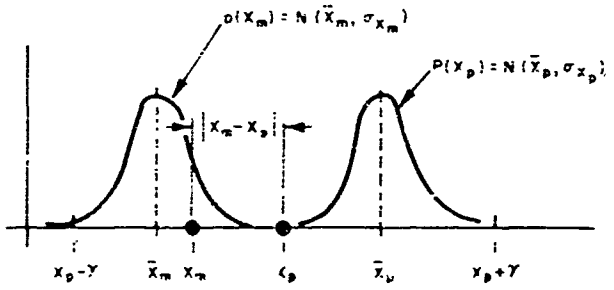

Fig. 3.13—Probability densities of X_p and X_m define i over correlation region

$$P[\text{break track}] = \int_{-\infty}^{-\gamma} P(\omega)d\omega + \int_{\gamma}^{\infty} P(\omega)d\omega , \tag{3.26}$$

which reduces to

$$P[\text{break track}] = 1 - \frac{1}{2}\,\text{erf}\left[\frac{\gamma - \bar{\omega}}{\sqrt{2}\,\sigma_\omega}\right] - \frac{1}{2}\,\text{erf}\left[\frac{\gamma + \bar{\omega}}{\sqrt{2}\,\sigma_\omega}\right] . \tag{3.27}$$

This probability can be bounded by

$$P[\text{break track}] \leq 1 - \text{erf}\left[\frac{\gamma - |\bar{\omega}|}{\sqrt{2}\,\sigma_\omega}\right] , \tag{3.28}$$

where

$$\bar{\omega} = \bar{X}_m - \bar{X}_p = f(\alpha, \beta, T, \bar{X}_m)$$

$$\sigma_\omega^2 = \sigma_{X_p}^2 + \sigma_{X_m}^2 = f(\alpha, \beta, \sigma_{xm}) .$$

Observing Eq. (3.8) one might infer that the real problem in minimizing the probability of breaking track for a given T and measurement noise is that the target trajectory is so unpredictable. Digressing for a moment, we discuss below several possible approaches to filter design.

Some filters assume that the target trajectory is known and adjust α and β in an adaptive way such as to minimize the error, i.e., the Kalman filter (4). Some adaptive filters try to estimate the future bandwidth requirement (how fast $\bar{X}_m$ is varying) and adjust α and β to minimize the error. Other filters assume a given trajectory and minimize a cost function such as to determine β in terms of α (5). Other filters use fixed α and β, adjusted such that the error is minimized for the worst-case target trajectory; the error is bounded in this manner. In this author's opinion many of the types of filters discussed are not well suited to track-while-scan radar operation. Most of the difficulty seems to arise from assuming a priori target trajectories or making future predictions based upon too little information. A filter design will be discussed in a subsequent report.

3.7 Some Examples

The α-β tracker is used to track the highly maneuverable targets described in Section 2.4. The true and predicted range and azimuth are plotted vs time in Figs. 3.14 through 3.17. The correlation region was made sufficiently large such that the track would not be broken. The sampling time is 4 sec. Two different values of α and β were used. The standard deviation of range and azimuth noise are 250 ft and 0.52 degrees, respectively. The filtered-noise standard deviation σ_{xp} is shown with the predicted position. The measurement noise of the true trajectory is not shown since it tends to make the graph difficult to read.

Observing these figures we find that the lightly filtered case had less error in the mean but a larger standard deviation σ_{xp} than the more heavily filtered case

The same tracking situation as found in Fig. 3.14 is again shown in Fig. 3.18 except that the sampling time is reduced to 1 sec. One finds that the mean of the predicted

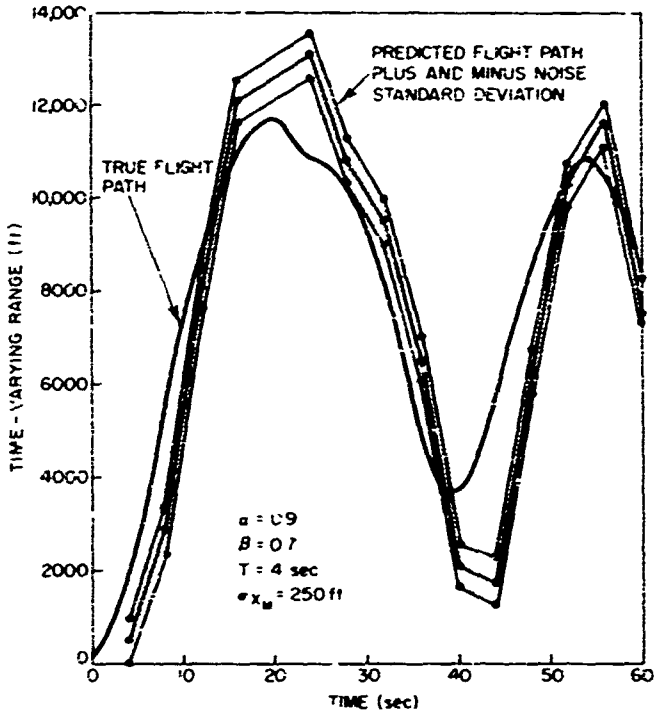

Fig. 3.14—Comparison of true and predicted signals for a highly maneuverable target

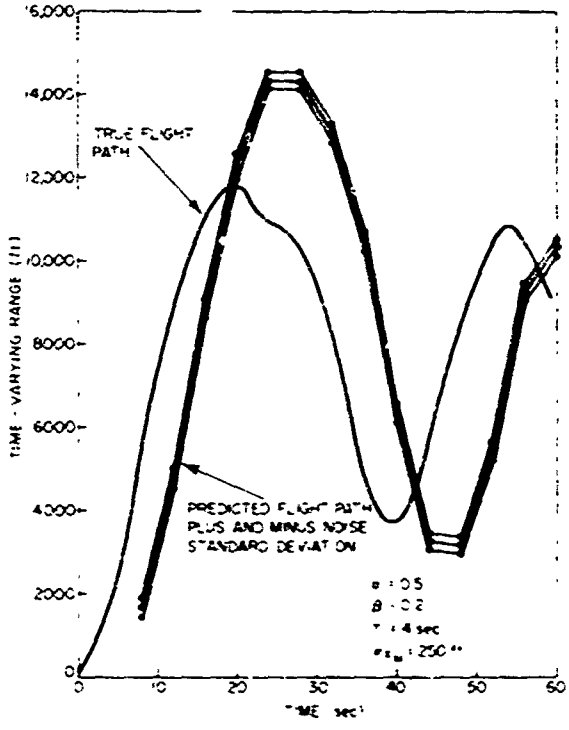

Fig. 3.15—Comparison of true and predicted signals for a highly maneuverable target

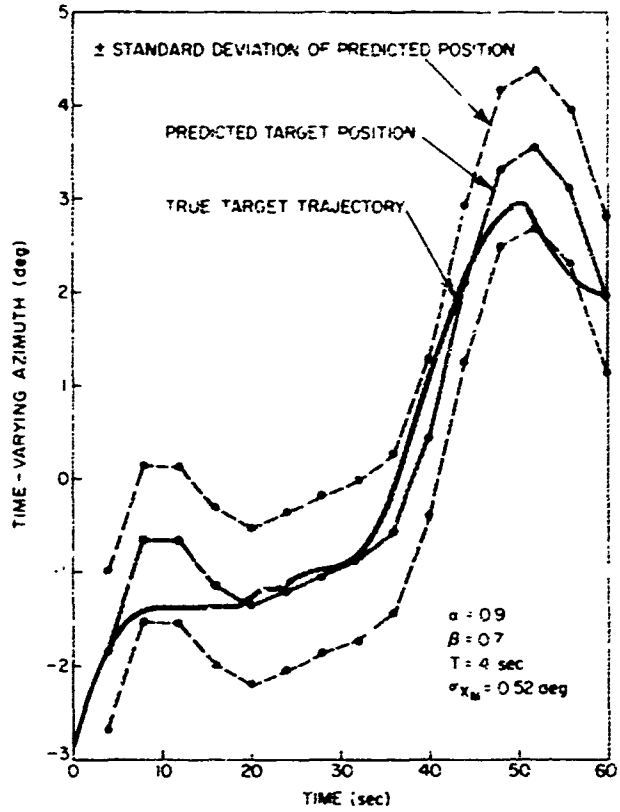

Fig. 3.16—Comparison of true and predicted azimuths for a highly maneuverable target

position tracks very close to the true trajectory (the standard deviation of the noise is the same as found before). This agrees with the theory in that a decrease in sampling time results in improved system performance. The same effect could be achieved if the target did not maneuver quite so violently such that the frequency content of the signal was less. This example shows how critical it is to know the frequency content of the target trajectory in order to design a good tracking system.

3.8 Discussion of Results

The behavior of the α-β tracker excluding the effects of false targets and fades was discussed. Although the analysis was quite straightforward, no reasonable way of adjusting α-β to minimize the probability of breaking track for a given γ was found. This difficulty arose from the fact that the probability of breaking track depended on the target trajectory and therefore the minima would be different for each trajectory. Adaptive and worst-case design solutions were mentioned. Several examples were given to illustrate the theory.

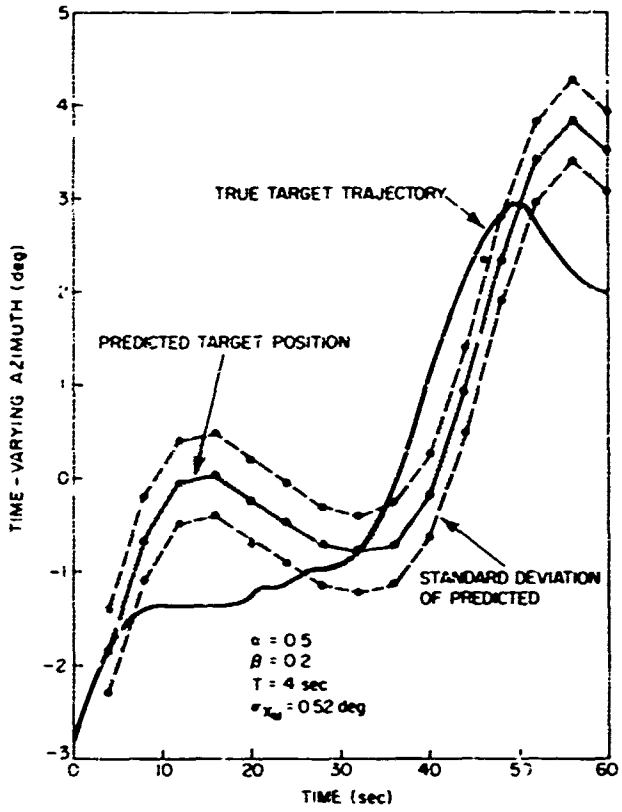

Fig. 3.17—Comparison of true and predicted azimuths for a highly maneuverable target

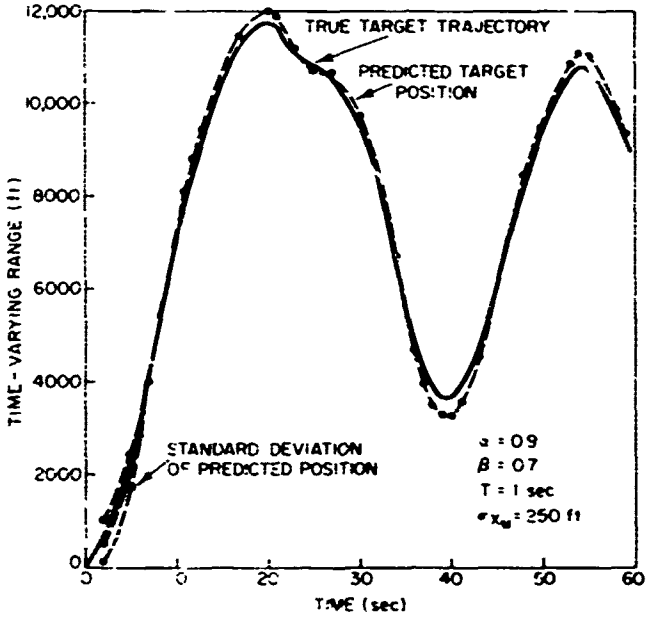

Fig. 3.18—Comparison of true and predicted ranges for a highly maneuverable target

4.0 SYSTEM LIMITATION DUE TO CLUTTER

As seen in the previous section one could make the probability of breaking track as small as one wishes by making the correlation region larger. In reality this is not the case because false targets caused by clutter or other targets place a basic limitation on this quantity. This effect is investigated next.

4.1 Average-Target Strategy

It is not known, at least to this author, what constitutes an optimum strategy for processing multiple targets within the correlation region nor how one would construct such a procedure. As an alternative to searching for an optimum processor, a strategy is postulated and analyzed.

It is assumed that any target present in the correlation region is an equally likely candidate for being the true target. In other words no a priori knowledge is available and the measurements are indistinguishable. Since it has been assumed that all targets are equally likely, the information from all targets will be used. The strategy postulated to achieve this goal is to average the position of all the targets in the correlation region: i.e.,

$$X_i^N = \frac{\left[X_m^N + \sum_{i=1}^{K} (X_p^N + n_i)\right]}{(K+1)}, \tag{4.1}$$

where

K = number of false targets in correlation region
n_i = zero mean uniform noise shown in Fig. 4.1.

X_i^N becomes the filter input rather than X_m^N as previously discussed. The filter equations can be written as

$$[X]^N = \underline{A}[X]^{N-1} + B[X_i]^N \tag{4.2}$$

$$[X_i]^N = \frac{\left[X_m^N + \sum_{i=1}^{K} (X_p^N + n_i)\right]}{(K+1)} \tag{4.3}$$

$$[X_p]^N = \underline{C}[X]^{N-1}. \tag{4.4}$$

Equations (4.2) and (4.3) are combined, yielding

$$\begin{bmatrix} X_s \\ V_s \end{bmatrix}^N = \begin{bmatrix} \left(1 - \frac{\alpha}{K+1}\right) & \left(1 - \frac{\alpha}{K+1}\right)T \\ -\frac{\beta}{(K+1)T} & \left(1 - \frac{\beta}{K+1}\right) \end{bmatrix} \begin{bmatrix} X_s \\ V_s \end{bmatrix}^{N-1} + \begin{bmatrix} \frac{\alpha}{K+1} \\ \frac{\beta}{T(K+1)} \end{bmatrix} \left[X_m^N + \sum_{i=1}^{K} n_i\right]. \tag{4.5}$$

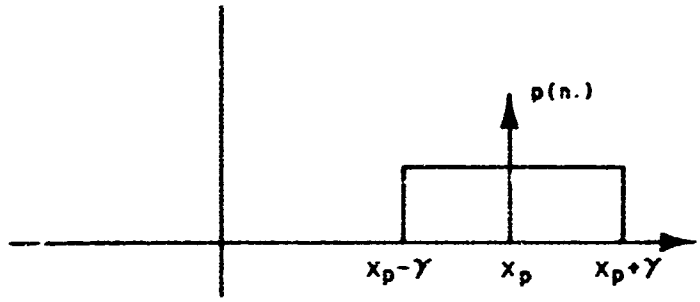

Fig. 4.1 Probability density function for clutter

Define α' and β' as

$$\alpha' = \frac{\alpha}{(K+1)} \tag{4.6}$$

$$\beta' = \frac{\beta}{(K+1)} \tag{4.7}$$

By using these definitions, Eq. (4.5) becomes

$$\begin{bmatrix} X_s \\ V_s \end{bmatrix}^N = \begin{bmatrix} (1-\alpha') & (1-\alpha')T \\ -\beta'/T & (1-\beta') \end{bmatrix} \begin{bmatrix} X_s \\ V_s \end{bmatrix}^{N-1} + \begin{bmatrix} \alpha' \\ \beta'/T \end{bmatrix} \left[X_m^N + \sum_{i=1}^{K} n_i \right] . \tag{4.8}$$

In this equation, the number of false targets K controls the amount of smoothing and the amount of measurement uncertainty.

The solution for the noise power of Eq. (4.5) is not nearly as easy as before. The reason is that K is a random variable. Equation (4.8) involves the product of two random variables and in general the probability density changes form from one iteration to the next. For this reason, only special solutions will be found.

4.2 Noise Characteristics for Given Clutter Conditions

Special solutions to Eq. (4.8) can be obtained by assuming that K is a deterministic sequence. For example,

1 0 0 0 0 1 0 0 0 0 1 0 0 . . .

4 4 0 0 4 4 0 0 4 4 0 . . . . . .

The equation becomes a stochastic difference equation with time-varying coefficients. In addition, the uniform probability density of the clutter is approximated as gaussian with the variance set equal to the variance of a uniform variable. The covariance equations are found in the same manner as before, i.e.,

$$\begin{bmatrix} P_{11} \\ P_{12} \\ P_{22} \end{bmatrix}^N = \begin{bmatrix} (1-\alpha')^2 & 2(1-\alpha')^2 & (1-\alpha')^2 \\ -\beta'(1-\alpha') & (1-2\beta')(1-\alpha') & (1-\beta')(1-\alpha') \\ \beta'^2 & -2\beta'(1-\beta') & (1-\beta')^2 \end{bmatrix} \begin{bmatrix} P_{11} \\ P_{12} \\ P_{22} \end{bmatrix}^{N-1}$$

$$+ \begin{bmatrix} \alpha'^2 \\ \alpha'\beta' \\ \beta'^2 \end{bmatrix} \left[\sigma_{X_m}^2 + \frac{K}{(K+1)^2} \sigma_{n_i}^2 \right], \tag{4.9}$$

where

$\alpha' = \alpha/(K+1)$
$\beta' = \beta/(K+1)$
$\sigma_{n_i} = \gamma/\sqrt{3}$
K = a deterministic sequence taking on the value of the number of false alarms at each iteration.

The following terms are defined:

$$\sigma_0 = \frac{\sigma_{X_p}}{\sigma_{X_m}} \tag{4.10}$$

$$\sigma_c = \frac{\sigma_{n_i}}{\sigma_{X_m}} \tag{4.11}$$

The predicted noise power is plotted vs time, for various conditions, in Figs. 4.2 through 4.9.

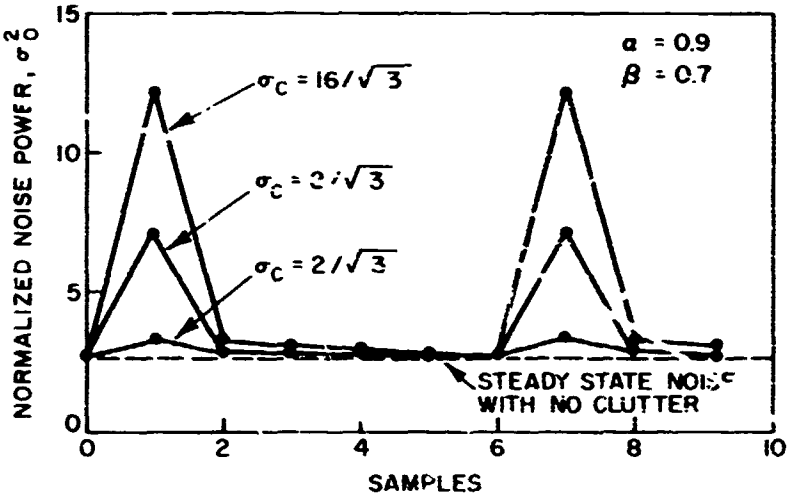

Fig. 4.2—Noise power as a function of time for sequence 10000010 . . .

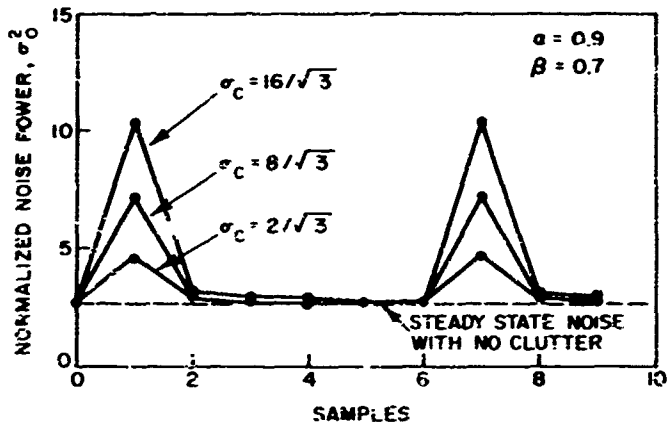

Fig. 4.3—Noise power as a function of time for sequence 40000040 . . .

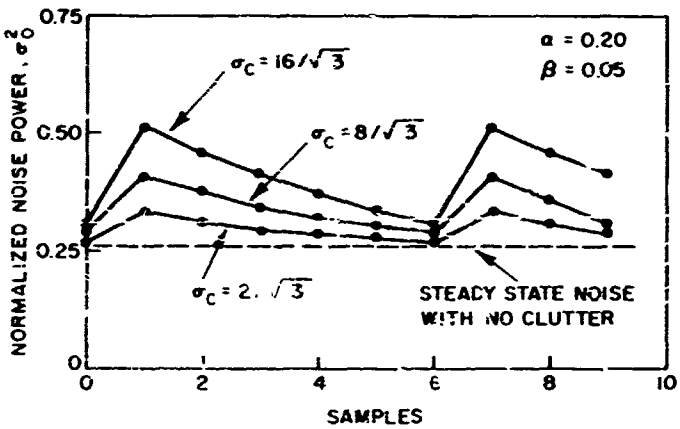

Fig. 4.4—Noise power as a function of time for sequence 10000010 . . .

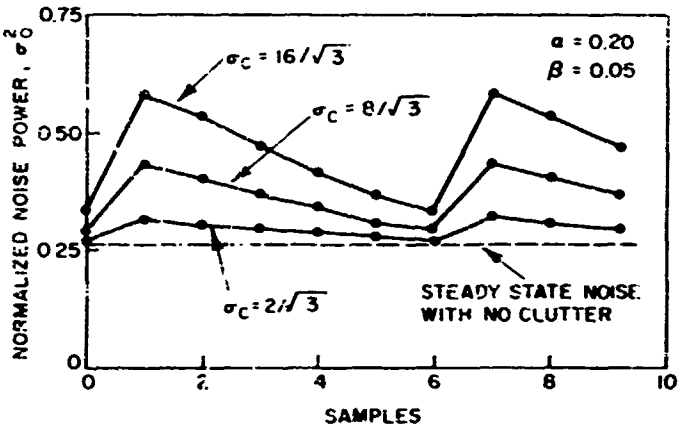

Fig. 4.5—Noise power as a function of time for sequence 40000040 . . .

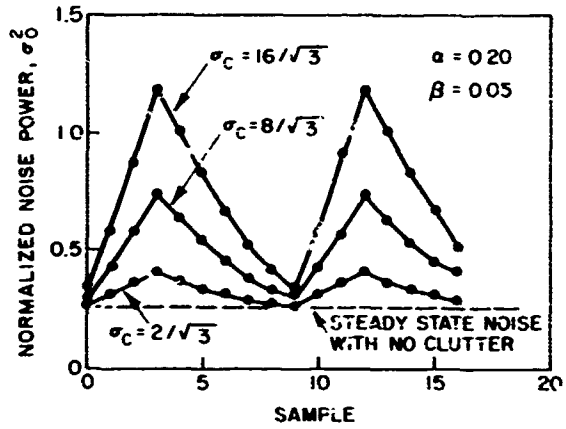

Fig. 4.6—Predicted noise power as a function of time for sequence 11100000011100 . . .

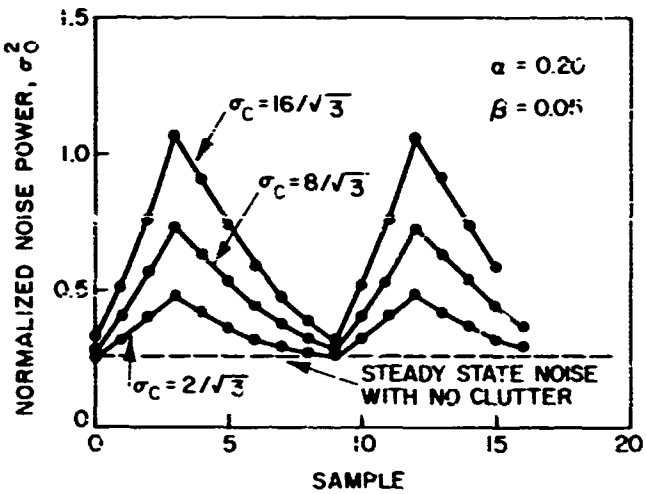

Fig. 4.7—Predicted noise power as a function of time for sequence 44400000044400 . . .

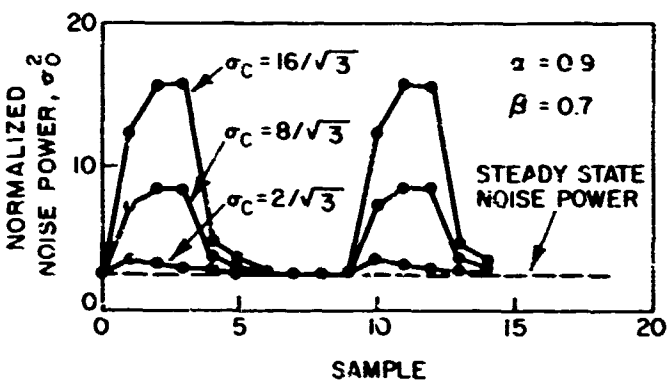

Fig. 4.8—Noise power as a function of time for sequence 11100000011100 . . .

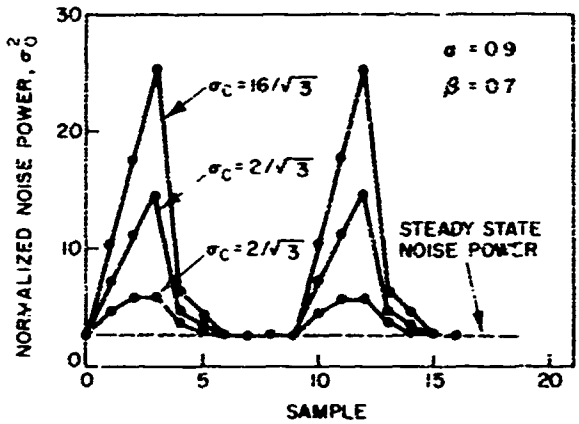

Fig. 4.9—Noise power as a function of time for sequence 44400000044 40 . . .

These figures show that when false targets appear periodically then a steady state solution exists for the noise power of the predicted position. The noise power increases during the time the clutter is present (it will be shown later that the noise power saturates at a given value in extended clutter), and drops back to its steady state value after the false targets are removed. In all cases it was found that when the correlation region size became larger as indicated by σ_c, the predicted noise power became larger during the period of the false alarms. The heavy smoothing case ($\alpha = 0.2$, $\beta = 0.05$) was generally less noisy than the light smoothing ($\alpha = 0.9$, $\beta = 0.7$) case. The sequences with *extensive* clutter (more than one false alarm in a row) were generally much more noisy than the single false alarm case.

If the sequences are such that K is the same value for all sampling instances, the predicted noise power saturates at a given value. These results are shown in Figs. 4.10 and 4.11. These figures indicate that larger correlation regions, more false alarms, and lighter damping all result in larger predicted noise power.

4.3 Deterministic System Behavior Under Clutter Conditions

If one either finds the mean value or eliminates the noise in the system described by Eq. (4.8) one has the following equation:

$$\begin{bmatrix} X_s \\ V_s \end{bmatrix}^N = \begin{bmatrix} (1-\alpha') & (1-\alpha')T \\ -\beta'/T & (1-\beta') \end{bmatrix} \begin{bmatrix} X_s \\ V_s \end{bmatrix}^{N-1} + \begin{bmatrix} \alpha' \\ \beta'/T \end{bmatrix} X_m^N . \tag{4.12}$$

The system is excited with a sinusoid and the root mean square error is found in the same manner as described in Section 3.5. The only difference in the solutions obtained here is that α' and β' vary from sample to sample according to a deterministic sequence in K; i.e.,

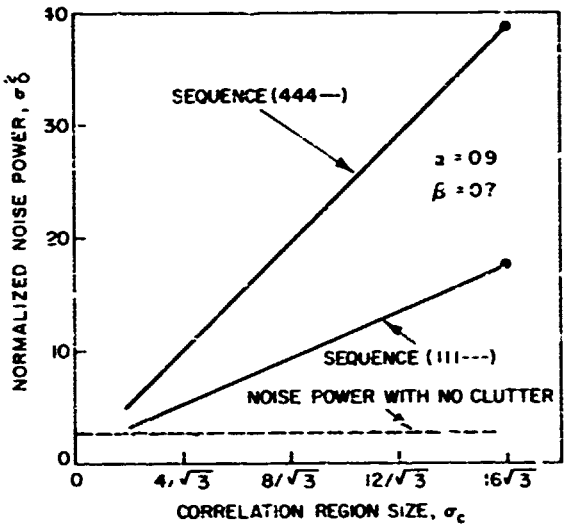

Fig. 4.10—Steady state normalized noise power as a function of correlation region size for two different sequences

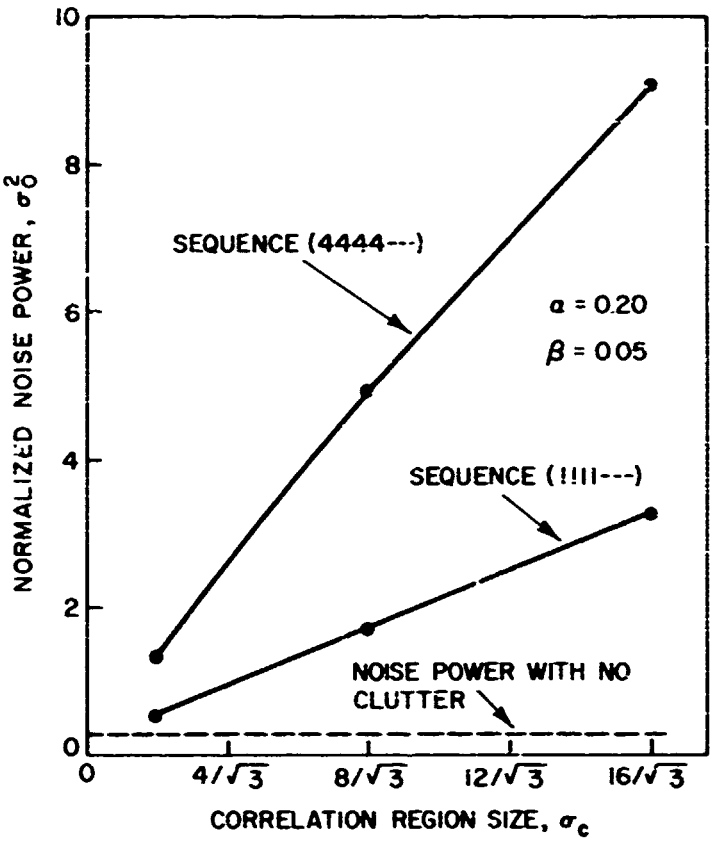

Fig. 4.11—Steady state normalized noise power as a function of correlation region size for two different sequences

$$\alpha' = \frac{\alpha}{K+1}$$
$$\beta' = \frac{\beta}{K+1}, \tag{4.13}$$

where

$$K = 11000110001100\ldots$$

The errors are shown as a function of various false alarm sequences and parameters α and β in Figs. 4.12 and 4.13.

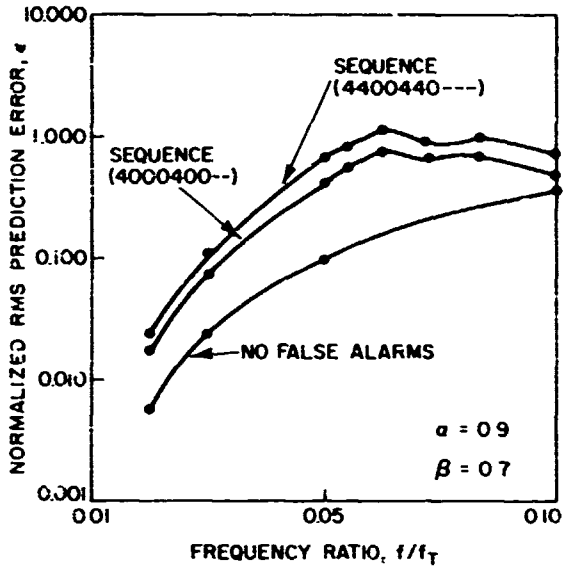

Fig. 4.12—Mean value frequency response under false alarm conditions

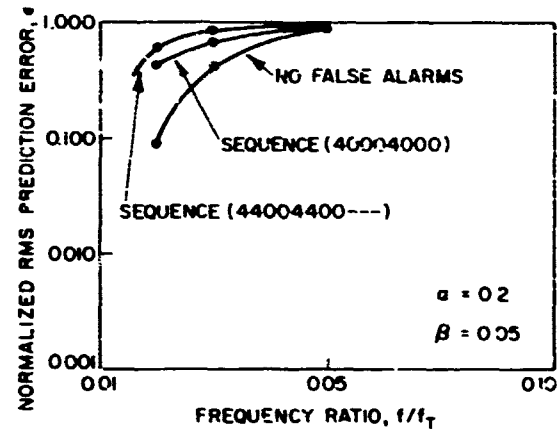

Fig. 4.13—Mean value frequency response under false alarm conditions

It is found that the error in the mean grows as the number of false alarms increases. Of course, it is again found that as the sampling frequency increases or the excitation frequency decreases the errors are less. Also, the more lightly filtered system has less error than the more heavily filtered system.

4.4 Probability of Breaking Track

In Section 3.6 the probability of breaking track was found to be

$$P[\text{break track}] \leq \frac{1}{2} - \frac{1}{2}\,\text{erf}\left[\frac{\gamma - |\bar{\omega}|}{\sqrt{2}\,\sigma_\omega}\right]. \tag{4.14}$$

In the presence of clutter both $|\bar{\omega}|$ and σ_ω increase, making the probability of breaking track worse.

It is not always possible to make the probability of breaking track smaller by making correlation region larger as can be seen from the following argument. As one increases the size of the correlation region, the chances of receiving one or more false alarms increases. At some point the probability of breaking track would start increasing with increasing γ due to the large errors set up by the false alarms. Thus for a given clutter environment, the probability of breaking track can not be made arbitrarily small.

4.5 An Example

The same tracking situation as shown in Fig. 3.16 is used except that in this case four false alarms per correlation region are assumed to occur at t = 16, 20, and 24 sec. The correlation region is assumed to be 16 times larger than the measured standard deviation. The resulting track is shown in Fig. 4.14.

One finds that when clutter is present, the filter has heavy smoothing and does not negotiate the turn well. In other words the mean of the predicted position is further in error. In addition, the standard deviation σ_{X_p} of the filtered noise grows during the time the false alarms are present due to the added noise. Of course if the heavy clutter would have appeared during a time that the target was not maneuvering so violently, the errors would have been much less. This suggests that the system could be improved by sampling faster. There is, however, an upper limit to this procedure, and that occurs when the clutter begins to be correlated.

4.6 Discussion of Results

An average-target strategy was postulated and analyzed. Because a general solution for the predicted noise power and deterministic tracking error is extremely difficult, only special solutions were found. It was found that the prediction noise increased when the amount of clutter increased, when the correlation region was made larger, and when the system used tighter filtering. In addition, the deterministic error grew as the clutter levels increased, as the system used heavier smoothing, and as the sampling frequency was decreased. It was argued that the probability of breaking track could not be made arbitrarily small in the presence of clutter by making the correlation region larger.

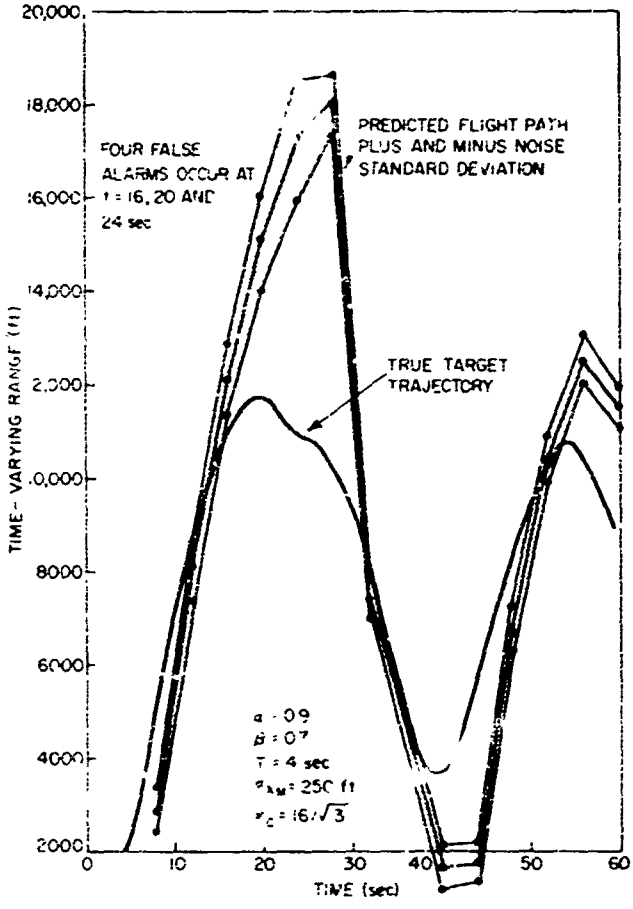

Fig. 4.14—Comparison of true and predicted ranges for a highly maneuverable target in the presence of clutter.

5.0 SYSTEM LIMITATION DUE TO FADES

Target fading can be caused by many factors of which the multipath effect is possibly one of the most troublesome. Considering this fading source only, one investigates the parameters that effect the interval of time during which the fade occurs. The effects of multipath fades on the system performance are analyzed by postulating a strategy and determining the characteristics of both the noise and the deterministic errors. It is assumed that no false targets are present.

5.1 Multipath Fading

The signal-to-noise ratio at the receiver can be computed from the radar range equation operating in the noise-limited region (6):

$$\left(\frac{S}{N}\right) = \frac{\Gamma_T G_T G_R \sigma \lambda^2 F_T^2 F_R^2}{(4\pi)^3 K T_s B_N R^4 L}, \tag{5.1}$$

where the pattern propagation factors F_T and F_R are due to the multipath effect. They are found by adding the electric field from both the direct path E_d and reflected path E_r as shown in Fig. 5.1;

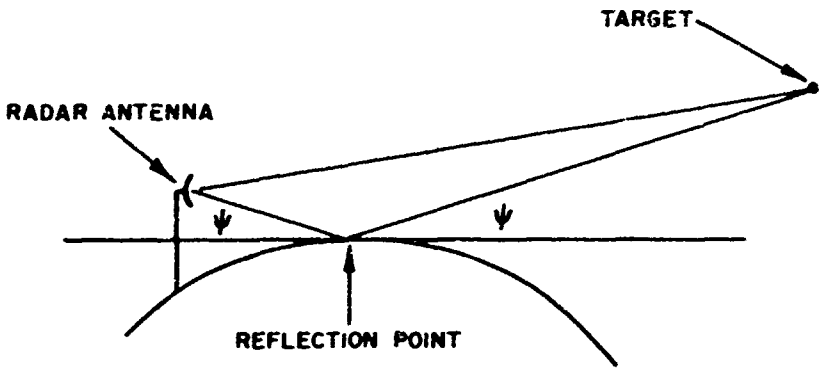

Fig. 5.1 Multipath effect

$$E = |E_d| + |E_r|e^{-j\alpha}$$

$$F = \left| 1 + \frac{|E_r|}{|E_d|} e^{-j\alpha} \right| \tag{5.2}$$

α = phase distance between the two paths .

These patterns have been studied quite extensively by Blake (7). Several antenna patterns reproduced from his work are shown in Figs. 5.2 through 5.4. Only two of the more important parameters, frequency and antenna height, which effect the patterns are listed with each figure.

An example is next considered. A target is flown from over the horizon toward the radar at a constant altitude of 10,000 ft. The radar is assumed to be a two-dimensional continuous-scanning search radar with an antenna height of 80 ft and a frequency of 1300 MHz. If the signal-to-noise ratio is above 13 dB (corresponds to a $P_d = 0.9$ and $P_{fa} = 10^{-6}$) a detection is assumed to be made; below 13 dB a fade is said to occur. For the target considered, the signal-to-noise ratio is assumed to be 17 dB at the center of the first lobe in which the target is detected, the lobe structure is computed using Blake's programs. The detection zones are shown in Fig. 5.5.

One finds that both the detection and fade zones decrease in size as the range is decreased. The main cause for this is that the angle of the lobe or angle between the lobes multiplied by the range gives the distance across the lobe or the distance between the lobes. These distances decrease as the range decreases. The fade zone decreases more rapidly than the detection zone with range. This can be attributed to an improved signal-to-noise ratio due to the decreased range. From this simple example one may estimate that fade zone distances may range from 10 naut. mi. to several thousand feet.

The length of time the target fades is given by

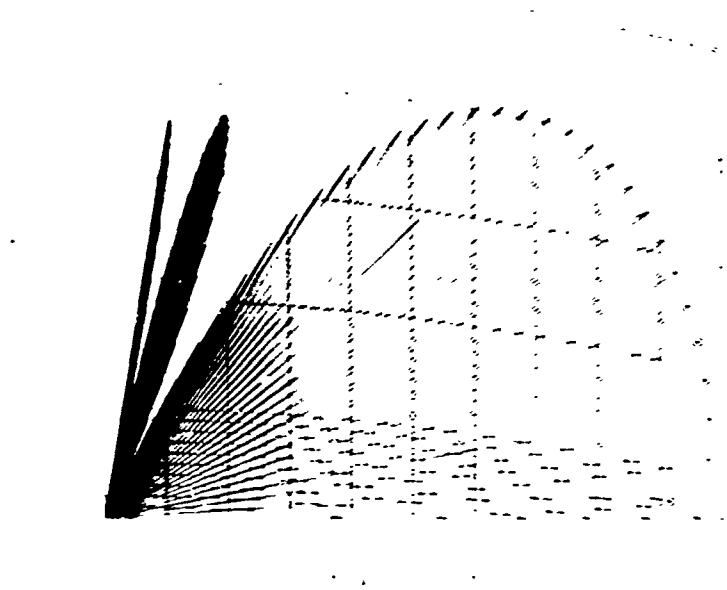

Fig. 5.2—Antenna pattern for an antenna height of 80 ft and frquency of 1000 MHz

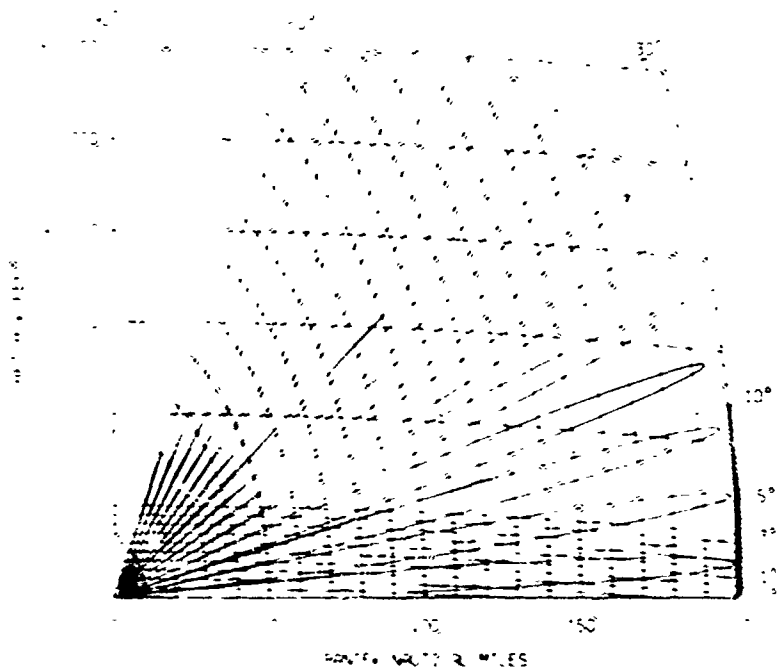

Fig. 5.3—Antenna pattern for an antenna height of 80 ft and frequency of 100 MHz

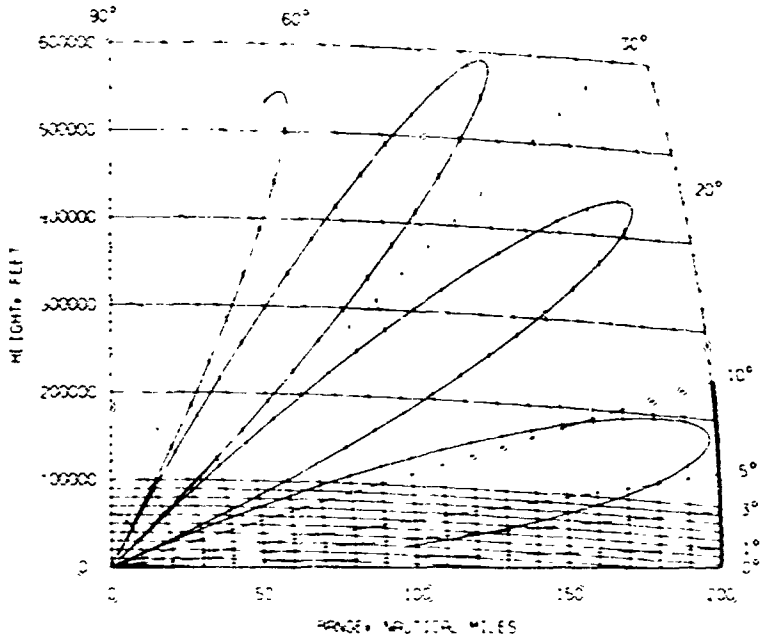

Fig. 5.4—Antenna pattern for an antenna height of 20 ft and a frequency of 100 MHz

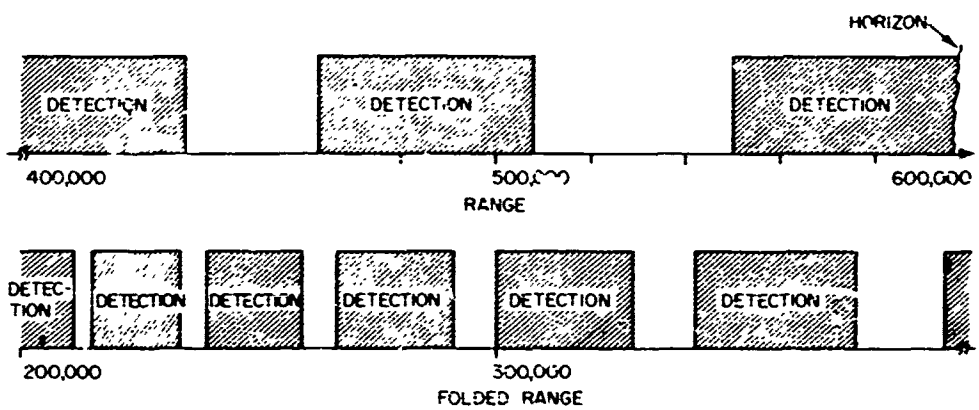

Fig. 5.5—Detection and fade zones vs range for a target at 10,000 ft, radar height 80 ft, frequency 1300 MHz, threshold S/N of 13 dB, and S/N ratio at 580,000 ft of 17 dB

$$T = \frac{\text{Distance between detection regions}}{\text{Target's radial velocity}} \quad (5.3)$$

This fade time is plotted vs radial velocity in Fig. 5.6 for a 10-naut.-mi. and a 10,000-ft fade zone.

Using the same example, we find that, at the far ranges where the fade zones are quite wide, the signal can fade from about 10 min at the low velocities to 0.5 min at the

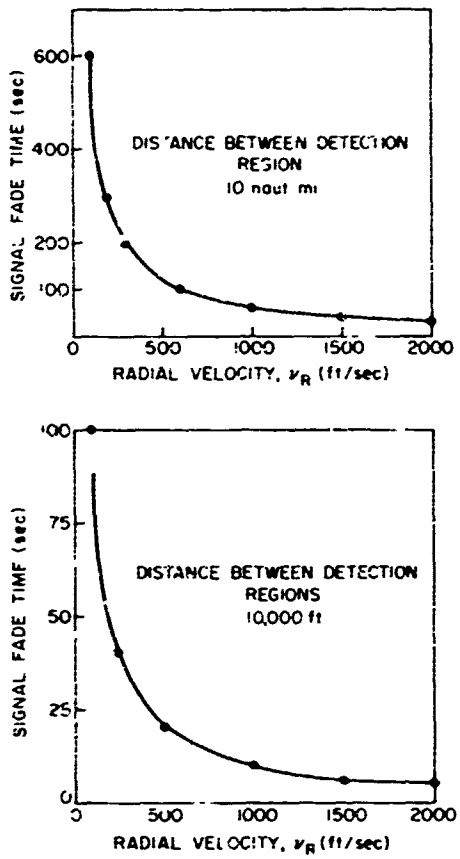

Fig. 5.6—Signal fade time vs radial velocity

high velocities. At the closer ranges where the fade zones are much narrower, the signal can fade from about a minute to several seconds or lower at the higher velocities.

It is desirable for later considrations to construct a sample sequence in which a "1" denotes a fade and a "0" a detection. Targets are flown through the detection and fade zones at various velocities. The position of the target is sampled every T seconds, according to the scan time of the radar. A 1 or a 0 is assigned to each sample instant according to whether the target is in the fade or detection zone. Several sequences are given in Figs. 5.7 and 5.8. The effects of fading sequences on the noise properties of the filter are now examined.

5.2 Predicted Value Strategy

When a fade occurs or no targets are present in the correlation regions, the usual policy to follow is to use the predicted coordinate as the measured one. This policy moves the target in a straight line trajectory at the last known velocity. This seems like a sensible policy, since there exists no a priori or current information about the status of the target.

The effects of this practice on the tracking equations are shown below. Equations (3.4) and (3.5 are rewritten as

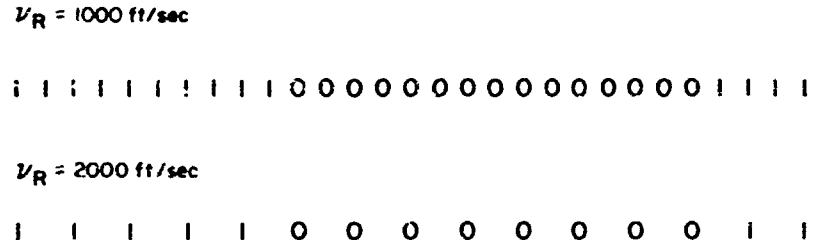

Fig. 5.7—Detection and fade sequences for fade zone lengths of 40,000 ft and detection zone lengths of 60,000 ft for two different radial velocities; T = 4 sec

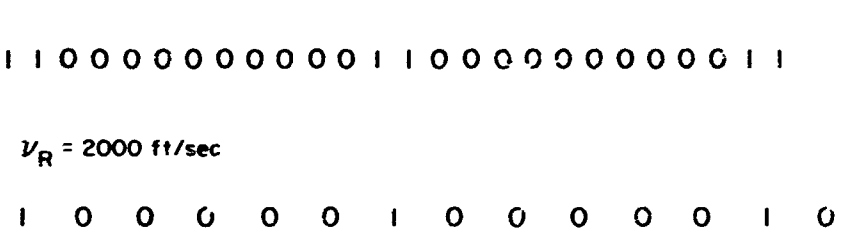

Fig. 5.8—Detection and fade sequences for fade zone lengths of 10,000 ft and detection zone lengths of 40,000 ft for two different radial velocities; T = 4 sec

$$\begin{bmatrix} X_s \\ V_s \end{bmatrix}^N = \begin{bmatrix} (1-\alpha) & (1-\alpha)T \\ -\beta/T & (1-\beta) \end{bmatrix} \begin{bmatrix} X_s \\ V_s \end{bmatrix}^{N-1} + \begin{bmatrix} \alpha \\ \beta/T \end{bmatrix} \begin{bmatrix} X_m \end{bmatrix}^N \tag{5.4}$$

$$\begin{bmatrix} X_p \end{bmatrix}^{N+1} = \begin{bmatrix} 1 & T \end{bmatrix} \begin{bmatrix} X_s \\ V_s \end{bmatrix}^N \tag{5.5}$$

Equation (5.5) is substituted into Eq. (5.4) to obtain

$$\begin{bmatrix} X_s \\ V_s \end{bmatrix}^N = \begin{bmatrix} 1 & T_s \\ 0 & 1 \end{bmatrix} \begin{bmatrix} X_s \\ V_s \end{bmatrix}^{N-1} , \tag{5.6}$$

where

$$X_p^N = X_m^N .$$

It can be seen that Eq. (5.6) is identical to Eq. (5.4) but with α and β set equal to zero. Therefore Eq. (5.4) describes the system under fading conditions where the parameters are time varying.

5.3 Filter Noise Characteristics Under Fading Conditions

The covariance Eqs. (3.18) and (3.19) are rewritten as

$$\begin{bmatrix} P_{11} \\ P_{12} \\ P_{22} \end{bmatrix}^N = \begin{bmatrix} (1-\alpha)^2 & 2(1-\alpha)^2 & (1-\alpha)^2 \\ -\beta(1-\alpha) & (1-2\beta)(1-\alpha) & (1-\beta)(1-\alpha) \\ \beta^2 & -2\beta(1-\beta) & (1-\beta)^2 \end{bmatrix} \begin{bmatrix} P_{11} \\ P_{12} \\ P_{22} \end{bmatrix}^{N-1} + \begin{bmatrix} \alpha^2 \\ \alpha\beta \\ \beta^2 \end{bmatrix} \sigma_{X_m}^2 \tag{5.7}$$

$$\sigma_{X_p}^2 = P_{11} + 2P_{12} + P_{22} . \tag{5.8}$$

The solutions for $\sigma_0 = \sigma_{X_p}/\sigma_{X_m}$ for various fading sequences, say 11001100..., are found such that if a one occurs, $\alpha = 0$, $\beta = 0$, and if a zero occurs, α and β take on their ordinary values. The solutions are shown in Figs. 5.9 through 5.13. Several general comments can be made concerning Figs. 5.9 through 5.13. First, the heavily smoothed filters (small α and β) are much less noisy than the lightly smoothed filters. In addition, the variances seem to become unstable if too many successive fades occur repeatedly.

It was found that the heavily damped filters were much more susceptible to instabilities than the lightly damped ones. A plausible explanation for this is as follows. When a fade occurs the estimate of the new position can become worse as time goes on. When

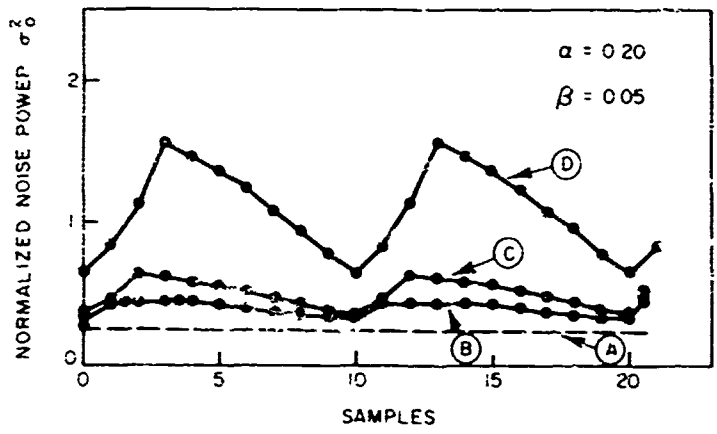

(A) NO FADES
(B) (1000000000001000--)
(C) (1100000000011000--)
(D) (1110000000011110000--)
(E) (11110000000111110000--)
(F) (111110000000111110000--) UNSTABLE SOLUTIONS
(G) ETC

Fig. 5.9—Normalized predicted noise power as a function of time for a given fading sequence

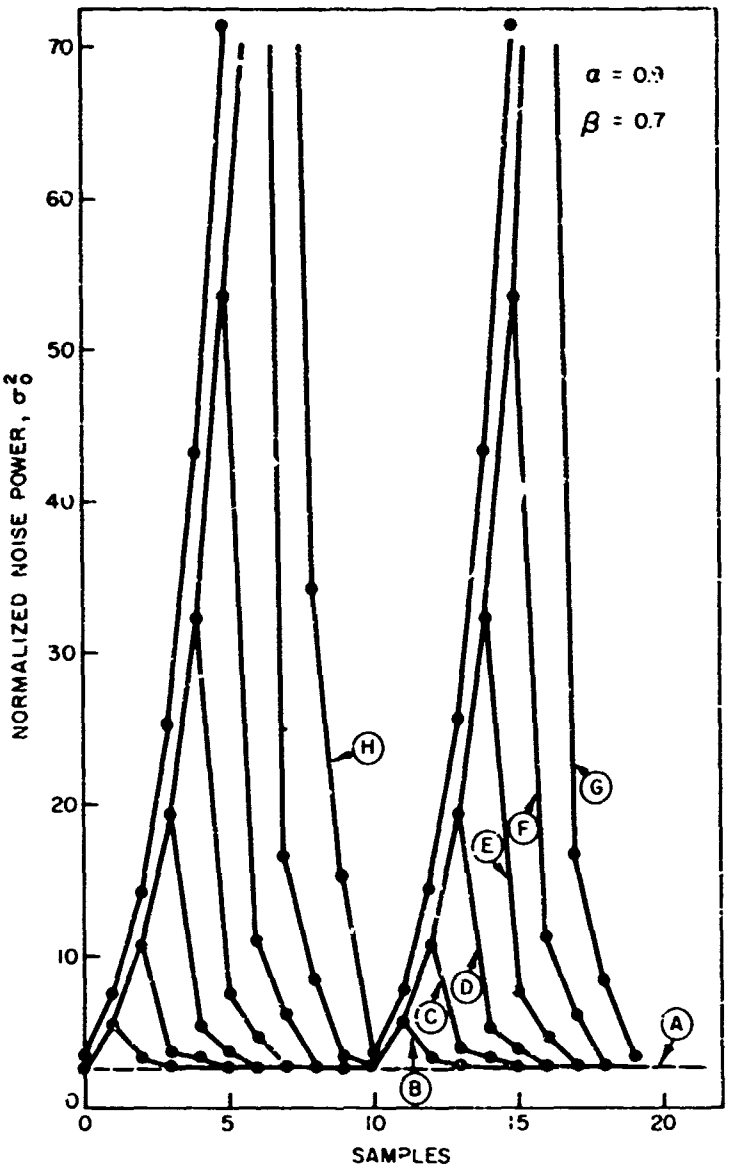

Ⓐ NO FADES

Ⓑ (100000000100--)

Ⓒ (1100000000110--)

Ⓓ (1111000000111--)

Ⓔ (1111100000011111--)

Ⓕ (1111110000011111--)

Ⓖ (1111111000011111100--)

Ⓗ (1111111000011111110--)

Ⓘ (1111111100011111111100--)

Ⓙ (ETC)

UNSTABLE SOLUTIONS

Fig. 5.10—Normalized noise power as a function of time for a given fading sequence

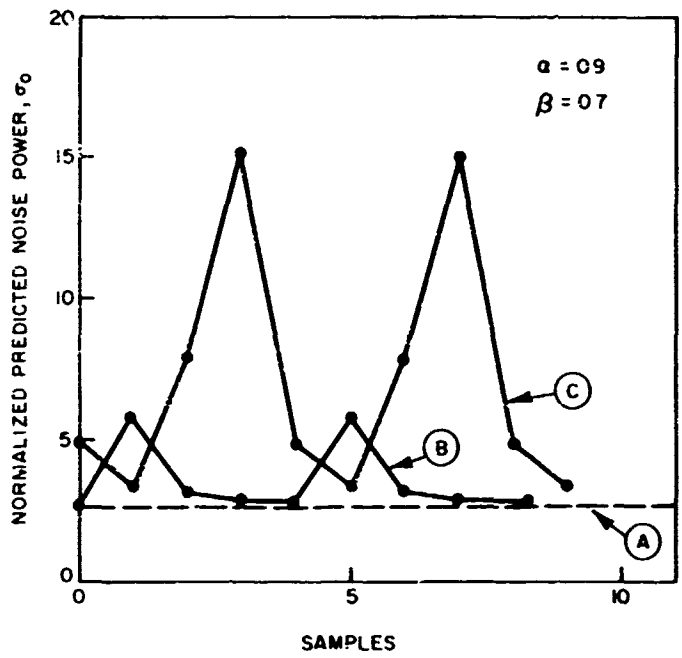

Fig. 5.11—Normalized predicted noise power as a function of time for various fading sequences: (A) no fades, (B) 10001000?0 . . . , (C) 11001100110 . . . , (D) 11101110 . . . unstable.

α = 0.2

β = 0.05

(A) NO FADES

(B) (1000100010--)

(C) (1100110011 0--)

(D) (1110111011 0--)

(E) ETC.

UNSTABLE SOLUTIONS

Fig. 5.12—Normalized predicted noise power as a function of time for various fading sequences: (A) no fades, (B) 1000100010 . . . , (C) 11001100110 . . . , (D) 111011101110 . . . , (E) etc. The last four are unstable.

a signal appears the heavily damped system recovers very slowly and only a poor estimate of the velocity and new position is found before a fade again occurs. If too many fades occur, the estimate continues to become worse. The lightly smoothed system recovers more rapidly after a fade and thus can handle longer fade sequences without becoming unstable.

It can also be observed that as the number of fades increases the noise power increases rapidly. One could decrease this by sampling at a slower rate which yields fewer fades at the expense of deterministic error increases. Yet this can lead to trouble; Figs. 5.10 and 5.11 can be considered to be sampled at two different rates. One finds in Fig. 5.11 that

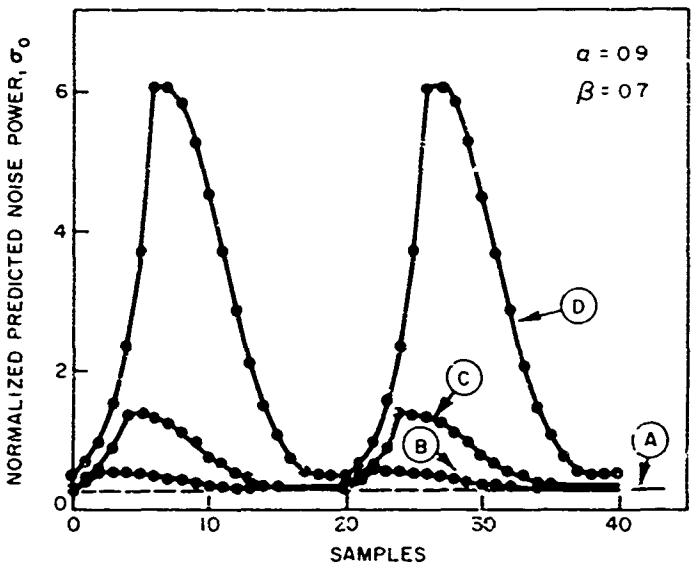

Fig. 5.13—Normalized predicted noise power as a function of time for various fading sequences: (A) no fades, (B) 11000000000000000001100 . . . , (C) 11110000000000000000111100 . . . , (D) 11111100000000000000111111 . . . , (E) 11111111000000000000111111111 . . . . (F) etc. (E) and (F) are unstable.

if the rate is slower the system becomes unstable for shorter fade zone lengths than it would have in Fig. 5.10. These comments are not necessarily true when the target moves through several fade zones between sampling times. Alternatively, rather than change the sampling rate, one could change the target's radial velocity and the same effect is observed.

If one increases the sampling rate, one in general reduces α and β. The effect of increasing the sampling rate with fades is to increase the noise, and the effect of reducing α and β is to reduce the noise. Unfortunately the prediction noise, when fading occurs, increases with sampling rate much faster than can be compensated for in changes in α and β as can be seen by comparing Figs. 5.9 and 5.13. The same effect would be observed by reducing the radial velocity of the target.

5.4 Deterministic Errors Under Fading Conditions

The error between the predicted and the true target position can probably best be studied by considering some examples. These are shown in Figs. 5.14 and 5.15. Figure 5.14 shows that for a realistic maneuver, the deterministic error between the true and the predicted coordinates was nearly 6 naut. mi. for about a medium-size fade zone. Figure 5.15 shows that even with fairly short fade zones as one might find in the region of 30 naut. mi. in range, one can easily be over a mile in error due to the deterministic process. If the target turned such that it flew parallel to the fade zone for some time, the errors could become enormous. Of course the total error is larger than that shown in these figures due to the addition of the random errors discussed in Section 5.3.

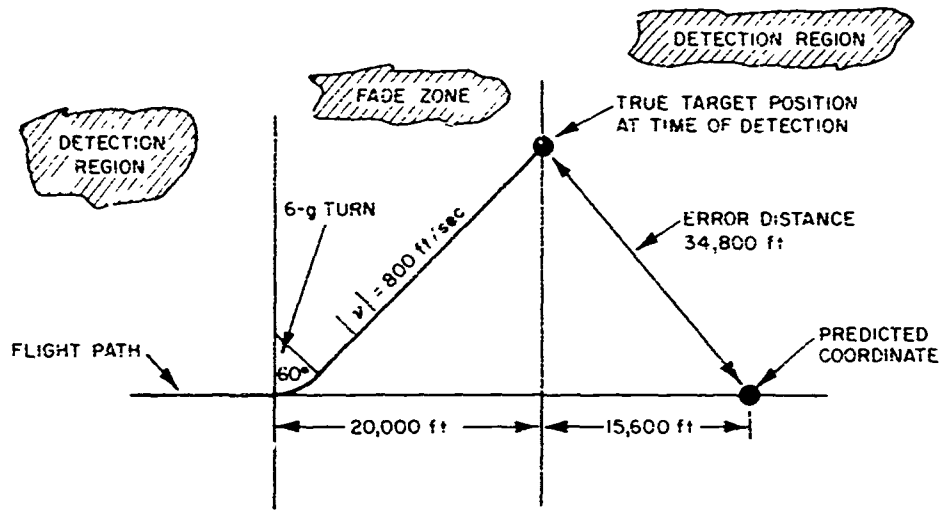

Fig. 5.14—Error between predicted and true coordinates during time of fade for Target 1

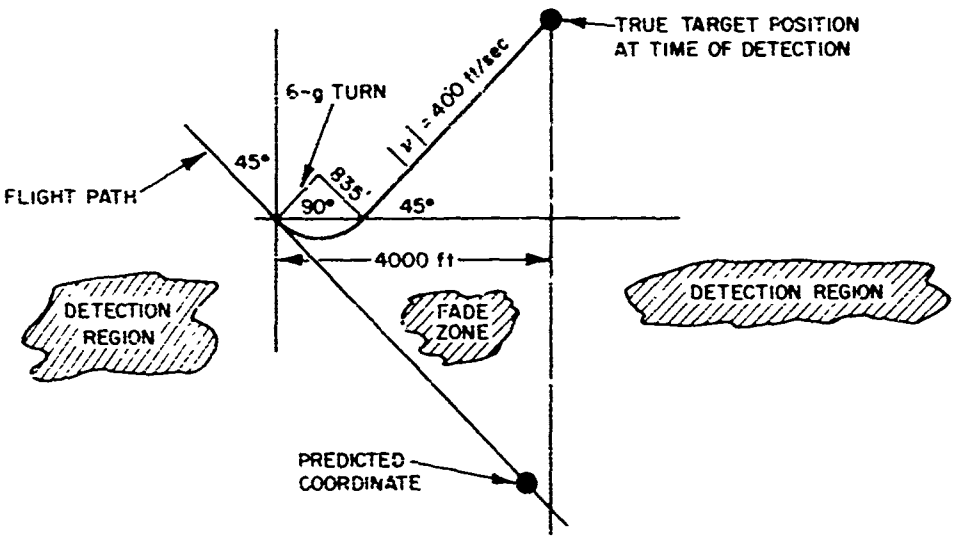

Fig. 5.15—Error between predicted and true coordinates during time of fade for Target 2

5.5 Probability of Breaking Track

Recall from Section 3.0 that the probability of breaking track depends on the variance of the predicted coordinate, the deterministic error between the true and predicted coordinates, and the size of the correlation region. Under long fading conditions it was found that the variance of the predicted coordinate grows rapidly and in addition the deterministic errors during fades can become quite large. This requires the correlation region to be quite large in order to obtain a reasonable probability of breaking track for many of the possible fading sequences and target trajectories. If the correlation region is large, the chances of tracking through regions containing false alarms become small. One could raise the threshold to eliminate some of the false alarms but then one does not detect the true target as often, thus making the fade problem worse.

5.6 Discussion of Results

The fading problem due to the multipath effect was reviewed and a procedure for the tracking equations to follow during the time of the fade was postulated. The variance of the predicted position was found for various fading sequences which depended for the most part on the distance between the lobes, the radial velocity, and the sampling time. The deterministic error between the predicted and true target positions was found for several examples. In a general way, the total error grows rapidly during a fade causing the correlation region size to grow in order to keep a track established. Of course, other considerations such as multiple targets, clutter, and resolution keep the correlation region from becoming too large.

6.0 CONCLUSIONS

The purpose of this report was to investigate the behavior of the α-β tracker under various conditions such as maneuvering targets, measurement noise, false targets, and fading conditions. Well-known elementary solution procedures were used throughout the report.

The probability of breaking track was found to depend on the measurement noise. α, β, sampling time, target trajectory, correlation region size, false alarm structure, and fading sequences. Excluding fades, the system error can be improved by increasing the sampling rate at least until the noise sources become correlated. For light filtering the noise was higher but the system tracked better in the mean. Conversely for heavy filtering, the noise was lower but the error was higher in the mean. The average-target strategy seemed like a good procedure to track through light or spotty clutter as long as the correlation region was small enough and the target did not perform extreme maneuvers during the time the false alarms were present. The predicted value strategy for fades probably would work reasonably well if the target did not maneuver just before or during the fade, if the fade time were reasonably short compared to the detection zone, and if the sampling time were slow enough. If these conditions are not met, quite large correlation regions are required which severely limit the ability to track through clutter and to resolve multiple targets. Examples were given throughout the report to indicate magnitudes of the functions that are typically found.

Secondary information can also be extracted from this report. The radar characteristics can be easily translated into tracking equation parameters. For example, pulse widths, beam widths, scanning rates, prf's, signal-to-noise ratios, antenna pattern characteristics due to multipath effects, clutter rejection capability, etc. can be translated into measurement accuracies, sampling times, fade conditions, and false alarm characteristics. Given a particular radar, one should be able, at least in a rudimentary way, to determine what types of tracks could be maintained.

ACKNOWLEDGMENT

I would like to thank Dr. G.V. Trunk for the many interesting discussions we had concerning this study over a period of several months during which this work was performed. I would also like to thank him for reading the entire manuscript and making critical comments concerning it.

REFERENCES

1. Schwartz, M., Bennett, W.R., and Stein, S., *Communication Systems and Techniques*, 1st ed., New York, McGraw-Hill, 1966.

2. Tou, J.T., *Digital and Sampled-Data Control Systems*, 1st ed., New York, McGraw-Hill, 1959.

3. Meditch, J.S., *Stochastic Optimal Linear Estimation and Control*, 1st ed., New York, McGraw-Hill, 1969.

4. Kalman, R.E., "A new Approach to Linear Filtering and Prediction Problems," *Trans. ASME, J. Basic Eng.* Ser. D, 82, 35-45 (Mar. 1960).

5. Benedict, T.R., and Bordner, G.W., "Synthesis of an Optimal Set of Radar Track-While-Scan Smoothing Equations," *IRE Trans. Automat. Contr.*, AC-7 (No. 4), 27-32 (1962).

6. Skolnik, M.I., ed., *Radar Handbook*, 1st ed., New York, McGraw-Hill, 1970.

7. Blake, L.V., "Machine Plotting of Radio/Radar Vertical-Plane Coverage Diagrams," NRL Report 7098, June 25, 1970.